

doi: 10.1111/sed.70024

Sedimentology (2025) 72, 1860-1898

A model for the concomitant early formation of dolomite and fibrous clays in coastal bay systems: Evidence from the Eocene (Paris Basin, France)

JULIEN TALON**† (D), PIERRE PELLENARD* (D), JEAN-MARC BAELE†, FLORENCE QUESNEL‡, JUSTINE BRIAIS‡, ALINA IAKOVLEVA§, CHRISTIAN DUPUIS†, LUDOVIC BRUNEAU* and EMMANUELLE VENNIN* (D) *Biogéosciences, UMR 6282 CNRS, Université Bourgogne Europe, Dijon 21000, France (E-mail: julien. talon@u-bourgogne.fr) (E-mail: pierre.pellenard@u-bourgogne.fr) †Geology and Applied Geology, University of Mons, Mons 7000, Belgium ‡Bureau de Recherches Géologiques et Minières (BRGM), Direction des Connaissances et Géomodélisation du Sous-sol (DCGS), Orléans 45000, France §Laboratory of Paleofloristics, Geological Institute, Russian Academy of Sciences, Pyzhevsky pereulok 7, Moscow 119017, Russian Federation

Associate Editors - Daniel Ariztegui and Mike Rogerson

ABSTRACT

Detailed analysis of Lutetian-Bartonian deposits in the Paris Basin ('Marnes et Caillasses' Formation) provides new evidence of concomitant magnesian fibrous clays (palygorskite and sepiolite) and early microcrystalline dolomite. Although relatively uncommon in sedimentary archives, palygorskite and sepiolite are found in a wide range of environments, from deep-marine to terrestrial. In coastal bay environments, these clay minerals can be formed under arid conditions, either by direct precipitation or by transformation from a precursor, often in association with carbonate. The concomitant formation of fibrous clays and dolomite remains poorly understood until now. Most models consider that fibrous clays form alongside calcite. More recently, it has been suggested that dolomite dissolution can facilitate fibrous clay formation during diagenesis. A new integrative model for concomitant dolomite and fibrous clay formation in coastal marine bay systems is proposed here, based on X-ray diffraction, organic carbon isotopes, electron microscopy, cathodoluminescence, and epifluorescence. In such systems, highly fluctuating hydro-biogeochemical conditions alternately favour the early formation of dolomite or fibrous clays. This study highlights, for the first time, the concomitant presence of three striking processes: (i) microbially influenced microcrystalline dolomite formation; (ii) detrital Al-Fesmectite transformation into palygorskite; (iii) dolomite dissolution, facilitating magnesium availability. These processes are favoured by the warm climate conditions of the Middle Eocene and a progressively restricted coastal bay environment related to regional regression. Based on geochemical and biostratigraphic data, this study also provides the first evidence of the Late Lutetian Thermal Maximum (LLTM) in coastal environments. During the LLTM, increased aridity punctuated by episodic floods linked to intensified run-off further exacerbated the already highly fluctuating hydrobiogeochemical conditions, thus favouring the early formation of dolomite and fibrous clays. These climate conditions, combined with basin confinement linked to Pyrenean deformation, may have facilitated the onset of a significant Eocene fibrous clay episode in NW Europe.

Keywords dolomite, LLTM event, magnesian minerals, microbial influence, palygorskite, Paris Basin.

INTRODUCTION

Palygorskite and sepiolite are hydrous magnesium silicate fibrous clay minerals, relatively rare in the rock record, where they reflect particular physico-chemical conditions. They can, however, be found in many different environments (Isphording, 1973; Singer, 1979; Singer & Galán, 1984; Galán & Singer, 2011), including deep-marine (Tazaki et al., 1986; Chamley, 1989), coastal lagoon (Weaver & Beck, 1977; Perri et al., 2018) and lacustrine (Lopez-Galindo et al., 1996) or other terrestrial environments (Singer & Norrish, 1974). These fibrous clay minerals are generally interpreted as markers of arid to semi-arid conditions in sedimentary processes (Chamley, 1989; Weaver, 1989; Fagel, 2007; Jones & Conko, 2011), but have also been associated with hydrothermalism (Fulignati, 2020). Different mechanisms have been proposed for palygorskite formation, including neoformation by direct precipitation in alkaline waters and soils, or transformation from a precursor such as smectite, illite-smectite mixed-layers (Trauth, 1977; Weaver & Beck, 1977; Suarez et al., 1994; Lopez-Galindo et al., 1996; Chen et al., 2004; Zaaboub et al., 2005; Xie et al., 2013) or chlorite (Hong et al., 2007). The presence of a precursor in palygorskite formation has been primarily inferred in these cases by transmission electron microscopy (TEM), in deep-sea (Tazaki et al., 1986) or terrestrial environments (Suarez et al., 1994), including lacustrine settings (Chen et al., 2004). Dissolution of poorly ordered dolomite, acting as a magnesium source, has been suggested as an alternative mechanism for palygorskite formation during various diagenetic stages (Inglès & Anadón, 1991; Ryan et al., 2019). By contrast, sepiolite is generally considered to form through direct precipitation from the solution (Pozo & Calvo, 2018).

The simultaneous presence of palygorskite and dolomite has often been taken to indicate a magnesium-rich environment (Weaver & Beck, 1977; Singer, 1984; Inglès & Anadón, 1991; Xie et al., 2013) and inferred in peritidal-to-shallow coastal or lacustrine settings (Weaver & Beck, 1977; Inglès & Anadón, 1991; Draidia et al., 2016; Kadir et al., 2016). Dolomite has

sometimes been described as microcrystalline and subhedral (Wen et al., 2020; Sánchez-Román et al., 2023) and is thought to have originated syn-sedimentarily or in association with early diagenetic processes (Weaver & Beck, 1977; Gillhaus et al., 2010; Wen et al., 2020). In shallow coastal environments, dolomite formation at low temperature and under surficial conditions is most likely mediated by microbial activity (Vasconcelos & McKenzie, 1997; Sánchez-Román et al., 2009a; Bontognali et al., 2010, 2014; Petrash et al., 2017; DiLoreto et al., 2021), but clay minerals may also facilitate its formation (Liu et al., 2019). In modern environments, especially in hypersaline lakes, the formation of magnesian fibrous clavs under the influence of microbial activity has also been suggested (Del Buey et al., 2018, 2021; Perri et al., 2018). Despite the apparent similarity between these processes, palygorskite formation mechanisms have generally considered calcite precipitation rather than dolomite formation, mainly in lacustrine or terrestrial environments other (Pozo Calvo, 2018). A comprehensive model explaining the mechanisms leading to the concomitant early formation of fibrous clays and microbially mediated dolomite in coastal environments remains to be developed.

In the Paris Basin, several fibrous clay episodes related to evaporitic deposits have been identified in the Palaeogene period (Pomerol, 1967), particularly associated with massive Priabonian gypsum deposits around Paris (Trauth, 1977). The first occurrence of palygorskite deposits of some importance in the Paris Basin is, however, recognized in the late Lutetian (Cavelier, 1963; Pomerol, 1967; Trauth et al., 1968; Thiry, 1989). This occurrence, associated with microcrystalline dolomite (Caillière et al., 1966; Fontes et al., 1970; Arnould et al., 1971) and gypsum (Sover, 1960; Toulemont, 1987), is identified in the 'Marnes et Caillasses' Formation (MCF), where the depositional environment has variously been described as lagoonal, sabkha-like or even lacustrine (Broekman, 1984; Fontes & Toulemont, 1987). At a global scale, the Eocene was marked by several hyperthermal events such as the Late Lutetian Thermal Maximum (LLTM), identified

1862 J. Talon et al.

open marine deposits (Intxauspe-Zubiaurre et al., 2018; Westerhold et al., 2020). The concomitance between hyperthermal events and the simultaneous development of fibrous clays and dolomite in the coastal environments of the Paris Basin provides the ideal opportunity to investigate the possible influence of climate on the formation of these magnesian minerals.

This study investigates the mechanisms driving the concomitant early formation of fibrous clay minerals and microcrystalline dolomite in a coastal marine bay setting, in relation to specific climate conditions, based on petrological observations (transmission and scanning electron microscopy (TEM and SEM), cathodoluminescence and epifluorescence) together with mineralogical (X-ray diffraction: XRD) geochemical ($\delta^{13}C_{org}$) analyses. Disentangling the relative impact of climate, depositional environment and palaeogeography on the processes leading to the formation of fibrous clavs and dolomite will provide important information about their distribution. For the first time, a comprehensive model is proposed to explain the concomitant, microbially mediated formation of palygorskite and dolomite in ancient coastal environments.

GEOLOGICAL SETTING

Palaeogeography of the Paris Basin

The intracratonic Paris Basin was open to the North Sea during the early Eocene, whereas the Ardenno-Rhenish and Vosges massifs to the east and the Massif Central to the south were emerged lands throughout the Eocene (Fig. 1A). To the west, a palaeo-Channel strait between the emerged Cornubian High and Armorican Massif intermittently connected the Paris Basin to the Atlantic Ocean (King, 2006). In relation to the Weald-Artois-Ardennes uplift (Pomerol, 1978; Gély, 1996, 2016) linked to Pyrenean deformation (Briais, 2015), the direct connection to the North Sea disappeared progressively during the late Lutetian and the Bartonian. During that period, as a result, the Paris Basin became a gulf primarily connected to the Atlantic Ocean (Fig. 1A).

Lithostratigraphy and biostratigraphy

In the Paris Basin, thermal subsidence led to the deposition and preservation of sediments during the Cenozoic (Brunet & Le Pichon, 1982), despite a very low accommodation rate (Guillocheau et al., 2000). During the Eocene, alternating siliciclastic and carbonate sediments were deposited in shallow epicontinental seas or terrestrial environments. A complex lithostratigraphy related to the numerous lateral facies variations has been developed since the 18th century (Mégnien & Mégnien, 1980; Gély, 2016; Egal, 2023). Figure 2 presents a concise view of the lithostratigraphic units spanning the late Ypresian-early Bartonian interval (~51) 39 Ma). The upper Ypresian siliciclastic system is followed by a major hiatus of at least 2 Myr (Pomerol, 1989; Briais et al., 2016; Steurbaut et al., 2016). A Lutetian inner carbonate platform system is described above, starting with a bed of coarse, calcareous, glauconitic sand ('Glauconie grossière' unit), diachronous at the scale of the Paris Basin, followed by three shallow marine, bioclastic limestone units ('Calcaire à Nummulites laevigatus', 'Calcaire à Ditrupa strangulata', 'Calcaire à Milioles et Orbitolites complanatus') representing the 'Calcaire grossier' Formation (Mégnien & Mégnien, 1980). The carbonate platform then passed to a restricted environment represented by the 'Marnes et Caillasses' Formation (MCF), described as a lacustrine to sabkha-like or lagoonal environment (Fontes & Toulemont, 1987), yet affected by marine incursions in the north-western part of the basin (e.g. 'Falun de Foulangues' unit; Cavelier & Le Calvez, 1965). A shorter hiatus, associated with emersion and karstification (Pomerol, 1989; Briais, 2015; Marie, 2023; Moreau, 2023), occurred during the early Bartonian, before the development of a siliciclastic coastal system ('Sables d'Auvers' and 'Sables de Beauchamp' units). Terrestrial and lacustrine environments and soils persisted throughout the period along the eastern and southern margins of the Paris Basin (Fig. 2; Blondeau, 1965; Thiry, 1989; Gély, 2016; Moreau et al., 2024). The Paris Basin is marked by a long-term Lutetian regression culminating during the MCF and ending with a period of regional emersion between the MCF and the 'Sables d'Auvers' unit (Briais, 2015; Moreau et al., 2024).

This study focuses specifically on the MCF, which consists primarily of dolomite and clayey limestone, with some clay beds and gypsum lenses that occasionally recrystallized into calcite and silica (Mégnien & Mégnien, 1980; Fontes & Toulemont, 1987; Toulemont, 1987). Large gypsum lenses provide the first evidence

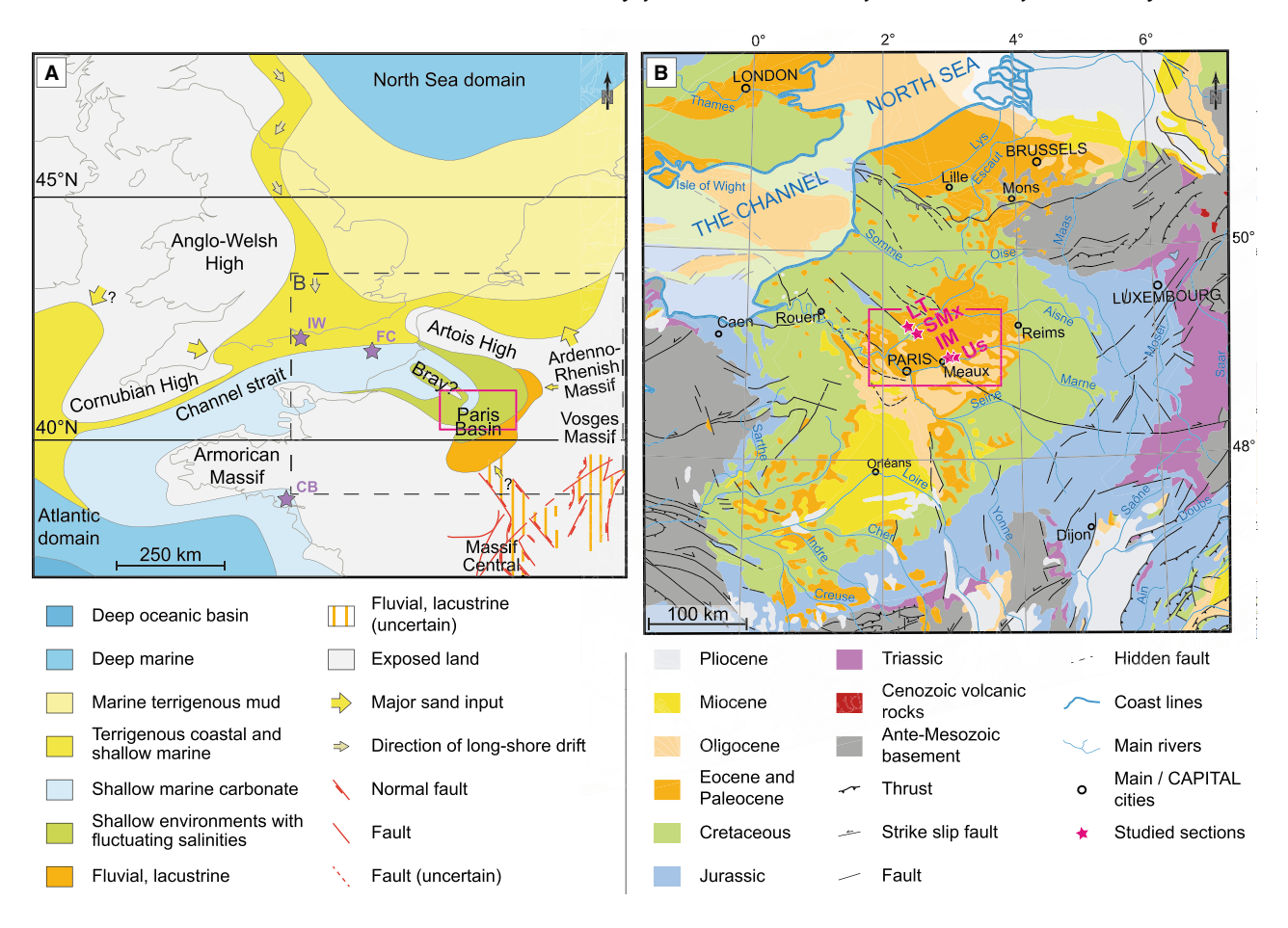


Fig. 1. Palaeogeographical map of the Paris Basin and surrounding areas (A) and geological map showing the studied sections in the Paris Basin (B). (A) Late Lutetian—early Bartonian palaeogeographical map of the NW European domain (modified from Meulenkamp et al., 2000, after Bignot et al., 1968 and Knox et al., 2010); purple stars indicate localities mentioned in the discussion: Foraminifera-rich deposits (with Alveolina elongata and abundant Nummulites) in the Channel Strait (FC), Isle of Wight (IW) and Campbon Basin (CB). (B) Geological map (modified from Asch, 2005 (IGME 5000); Quesnel et al., 2014; Iakovleva et al., 2021). Pink stars indicate the studied sections: Le Tillet (LT); Saint-Maximin (SMx); Isles-les-Meldeuses (IM); Ussy-sur-Marne (Us).

of evaporitic conditions in the Paris Basin during the Palaeogene (Arnould *et al.*, 1971; Toulemont, 1987).

The biostratigraphy of the Paris Basin during the end Ypresian—early Bartonian interval is mainly based on foraminifera and nannofossils. The upper Ypresian siliciclastic system has been assigned to Zone NP12 (nannoplankton biozonation; Aubry, 1986), but only the base of Zone NP13 has been identified locally (Steurbaut et al., 2016); the lowermost Lutetian platform carbonate corresponds to the upper part of Zone NP14 (Aubry, 1986), suggesting that most of zones NP13 and NP14 are missing. The presence of Nannotetrina fulgens alongside Braarudosphaera bigelowii, Discoaster barbadiensis,

D. boulangeri, D. saipanensis, Ericsonia formosa, Micrantholithus flos, Pemma rotundum, Reticulofenestra dictyoda, R. pseudogammation, Rhabdosphaera crebra and Zvgrhablithus bijugatus, but without Discoaster sublodoensis or Rhabdosphaera inflata identifies Zone NP15 in the upper part of the 'Calcaire à Nummulites laevigatus' unit (Aubry, 1986). This nannofossil biozonation is consistent with the presence of sometimes abundant Nummulites laevigatus, indicative of the lower Lutetian SBZ13 (shallow benthic foraminifera biozonation; Serra-Kiel et al., 1998). The simultaneous occurrence of Chiasmolitus solitus, Discoaster tanii nodifer and Reticulofenestra hillae without Reticulofenestra reticulata identifies the lower part of

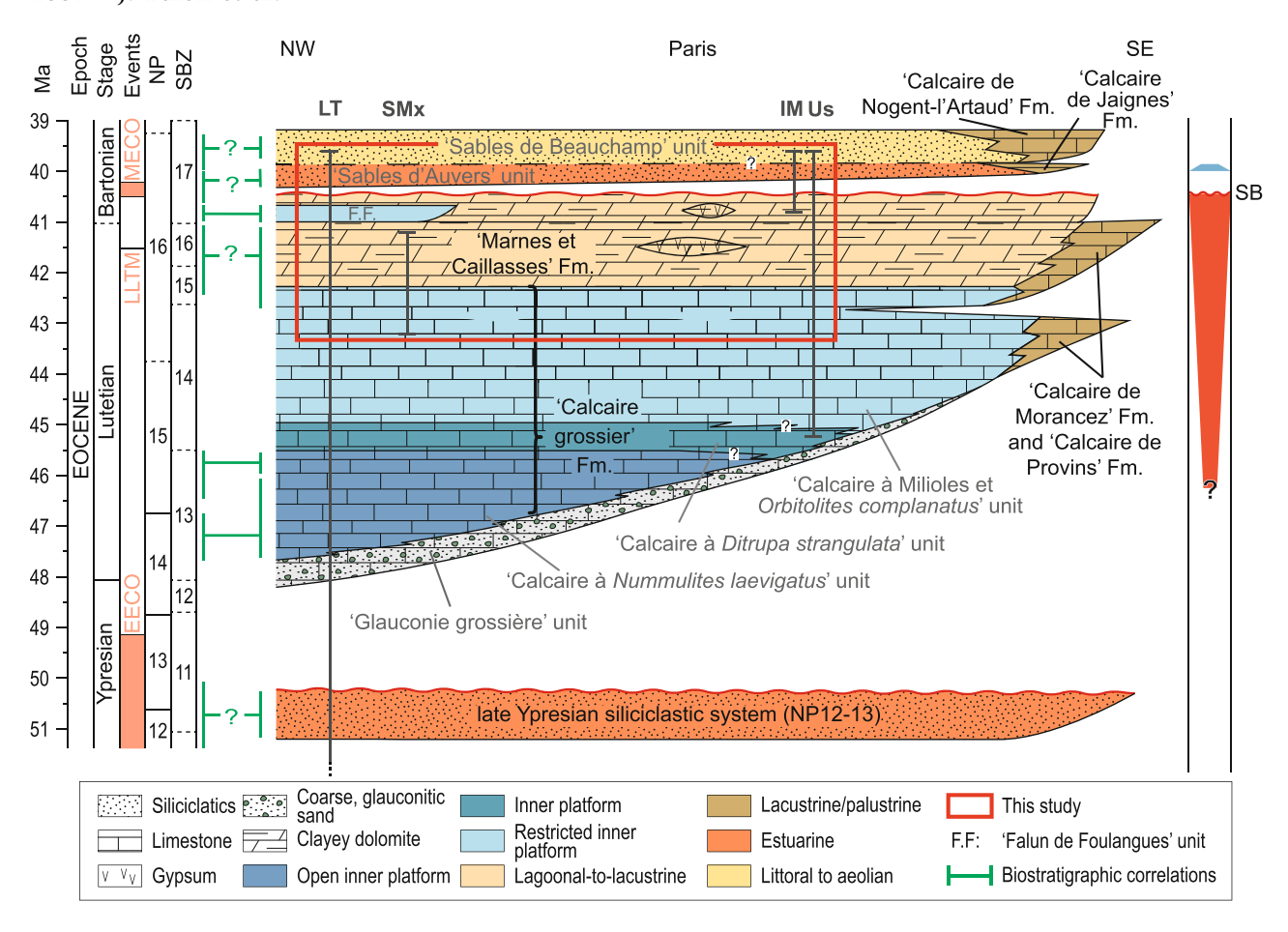


Fig. 2. Concise late Ypresian—early Bartonian lithostratigraphy and chronostratigraphy in the Paris Basin (modified from Gély, 2016 after Briais, 2015; Marie, 2023 and Moreau et al., 2024). Chronostratigraphic scale from GTS 2020 (Speijer et al., 2020). Hyperthermal events are from Rivero-Cuesta et al. (2019) for the MECO, Westerhold et al. (2018a) for the LLTM and Westerhold et al. (2018b) for the EECO. Long-term sequence stratigraphic framework after Briais (2015) and Moreau et al. (2024). EECO, Early Eocene Climatic Optimum; LLTM, Late Lutetian Thermal Maximum; MECO, Middle Eocene Climatic Optimum; NP, nannoplankton biozonation; SBZ, shallow benthic foraminifera biozonation. Stratigraphic range and approximate position of the studied sections: Le Tillet (LT); Saint-Maximin (SMx); Isles-les-Meldeuses (IM); Ussy-sur-Marne (Us).

Zone NP16 in the MCF (Aubry, 1986). The presence of Alveolina elongata in the Le Tillet core Calvez. 1968) identifies the (Serra-Kiel et al., 1998) in the 'Falun de Foulangues' unit. As the SBZ17 marks the lowermost Bartonian (Serra-Kiel et al., 1998), the MCF thus encompasses the late Lutetian-early Bartonian transition (Fig. 2). The co-occurrence of Discoaster bifax, D. distinctus, D. tanii nodifer, Chiasmolithus solitus, Reticulofenestra hillae and Neococcolithites dubius identifies Zone NP16 in the 'Sables d'Auvers' unit (Aubry, 1986). The presence of Reticulofenestra reticulata and Neococcolithites dubius and the absence of N. minutus together indicate the upper part of Zone

NP16 in the 'Sables de Beauchamp' unit (Aubry, 1986).

MATERIALS AND METHODS

Four sections (i.e. two outcrops and cores from two boreholes) were studied along a NW–SE transect (Fig. 1B). The Le Tillet borehole (drilled in 1966, 45 km north of Paris) spans 193.35 m, from the Upper Cretaceous Chalk to the 'Sables de Beauchamp' (SaB) unit (Cavelier, 1968). The Saint-Maximin outcrop (Les Longères des Haies–BPE Lecieux quarry, 10 km east of Le Tillet) encompasses the transition

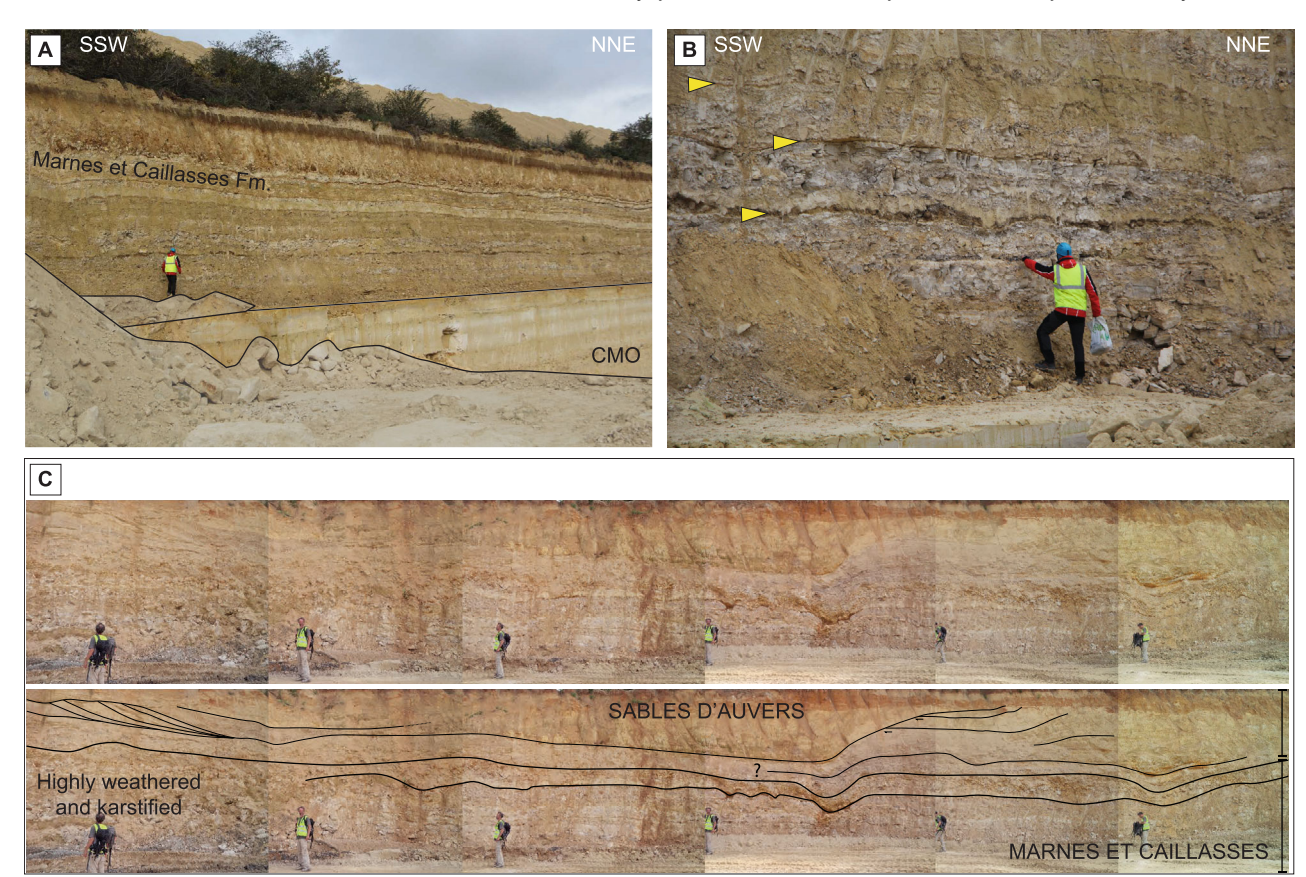


Fig. 3. Field views of the 'Marnes et Caillasses' Formation. (A) Saint-Maximin outcrop (Les Longères des Haies—BPE Lecieux quarry) illustrating the contact between the 'Calcaire à Milioles et *Orbitolites complanatus*' (CMO) unit and the 'Marnes et Caillasses' Formation. (B). Close-up view of the outcrop showing the alternation of clay intervals (yellow arrows) and more or less indurated carbonate beds in the 'Marnes et Caillasses' Formation. (C) Isles-les-Meldeuses outcrop (Sablière Capoulade quarry) showing the contact between the 'Marnes et Caillasses' Formation and the 'Sables d'Auvers' unit with evidence of deformation and karstification (Briais, 2015).

between the 'Calcaire à Milioles et Orbitolites complanatus' (CMO) unit and the MCF (Fig. 3A and B). The Isles-les-Meldeuses outcrop and the Ussy-sur-Marne borehole are located approximately 50 km north-east of Paris. The Isles-les-Meldeuses outcrop (sampled in 2013 in the Sablière Capoulade quarry, no longer exposed) encompasses the transition between the MCF and the 'Sables d'Auvers' (SaA) unit (Fig. 3C). The Ussy-sur-Marne borehole (drilled in 2013) spans 49 m, from the 'Calcaire à Ditrupa strangulata' (CD) unit to the Bartonian sands.

Microscopic and epifluorescence analyses of 42 thin sections (Table 1), using an Axioscope 7 (Carl Zeiss MicroImaging GmbH, Jena, Germany), at the Biogéosciences Laboratory (GISMO platform, Université Bourgogne Europe), complemented

macroscopic sedimentary facies observations. Cathodoluminescence analyses were performed on 34 of these thin sections, using a polarizing photomicroscope (Zeiss, Jena, Germany), in the Department of Geology and Applied Geology (University of Mons, Belgium). The cathodoluminescence (CL) images were generated by a cold-cathode CITL CL system (Cambridge Image Technology—model Mk5, UK), operated at 15 kV acceleration voltage, 500 µA beam current, with a current density of about 8 μA mm⁻². Cathodoluminescence images were captured with a Peltier-cooled digital colour camera (Lumenera model Infinity 3, Canada), set from 0.1 s to a few seconds exposure time, depending on CL intensity and microscope magnification. Multiple frame averaging was used to reduce noise. Colour calibration of the camera (white balance) was

1866 J. Talon et al.

Table 1. Summary of analyses performed in this study.

Site	Stratigraphic interval	Thick. (m)	TS	Cath.	Epi.	XRD	$\delta^{13}C_{\rm org}$	TEM	SEM	Pal.
Le Tillet	CMO unit to Sables de Beauchamp unit	39.7	17	17	17	66	64	5	3	0
Saint-Maximin	CMO unit to Marnes et Caillasses Fm.	7.5	16	11	16	40	19	5	14	0
Isles-les- Meldeuses	Marnes et Caillasses Fm. to Sables d'Auvers unit	21.5	0	0	0	22	16	6	4	3
Ussy-sur-Marne	CD unit to Sables d'Auvers unit	35.4	9	6	9	58	58	0	7	3
Total	d Advers difft		42	34	42	186	157	16	28	6

Thick.: Succession thickness; TS: Thin sections; Cath.: Cathodoluminescence; Epi.: Epifluorescence; Pal.: Palynology

performed using the blue-filtered, tungstenhalogen light source of the microscope.

The XRD analyses were conducted on 186 samples (Table 1) for bulk and clay fraction (<2 μm), using a D8 Endeavor diffractometer (Bruker, Billerica, Massachussetts, USA) with CuKα radiation, Lvnxeve XE-T detector under 40 kV voltage and 25 mA intensity (Biogéosciences laboratory, GISMO Platform, Université Bourgogne Europe). All samples were manually crushed in an agate mortar. To remove carbonates for the clay fraction analyses, approximately 10 g of powdered samples was agitated in 200 mL of osmosed water and a 0.2 mol L⁻¹ HCl solution was progressively added until the pH remained acidic (<2) after approximately 3 min, indicating that the reaction is complete. For very carbonated samples, a few drops of 6 mol L⁻¹ HCl solution were used instead of the 0.2 mol L⁻¹ solution. The residue was evacuated and neutralized by successive rinses until clay deflocculation was reached. Ammonia water was added to a few samples from Saint-Maximin and Isles-les-Meldeuses to help deflocculation. Clay-sized particles were extracted with a syringe, after decantation of the suspension for 95 min following Stokes law, and then centrifuged at 2300 g for 40 min. The resulting paste was then smeared on glass slides for clay orientation. Clay minerals were identified using their main diffraction peak (d_{001}) by combining the X-ray diffraction patterns obtained after each of the three treatments applied to each sample (Brown & Brindley, 1980; Moore & Reynolds, 1997): (i) air-drying, (ii) ethylene-glycol saturation overnight and (iii) heating at 490°C

for 120 min. Semi-quantification was performed using the MacDiff 4.2.6 software based on the peak area method, including deconvolution (Petschick, 2010). Estimated uncertainties for clay mineral and non-clay mineral proportions are between 1 and 3% (Hillier, 2000; Warr, 2022).

Scanning electron microscope (SEM) observations were conducted on 28 samples (Table 1) using a Hitachi SU8230 (Ibariki, Tokyo, Japan) in backscattered electron mode operating at 15 kV (ARCEN platform, Université Bourgogne Europe). Energy-dispersive X-ray (EDX) spectroscopy was used for qualitative chemical elemental analysis, with a ThermoFischer Scientific UltraDry 30 mm² (ThermoFischer Scientific, Waltham, Massachusetts, USA) combined with the Hitachi SU8230. Small sample pieces were cleaned using compressed air, mounted on aluminium stubs with electrically conductive carbon tape and coated with a thin (20 nm) layer of carbon. All rock samples were analysed at an accelerating voltage of 15 kV, with a working distance of 4 mm.

Transmission electron microscope (TEM) observations were performed on 16 clay fraction samples (Table 1). All samples were prepared by depositing a drop of the clay fraction diluted in a 2% butylamine solution onto a carbon-coated copper grid. Five samples were observed using a JEOL JEM-2100F microscope (JEOL (Europe) SAS, Croissy-sur-Seine, France), operating at 200 kV with a point-to-point resolution of 0.19 nm (ARCEN analysis platform, Université Bourgogne Europe), combined with EDX spectroscopy in TEM mode for qualitative

chemical elemental analysis, using a Bruker XFlash Detector 5030 spectrometer (Bruker France, Wissembourg, France) fitted on the JEM-2100F microscope, and 11 samples were observed using a Hitachi HT7800 (Hitachi High Tech Corp., Tokyo, Japan), operating at 100 kV with a point-to-point resolution of 0.36 nm (Dimacell analysis platform, INRAe, Dijon, France).

Organic carbon isotope analysis ($\delta^{13}C_{org}$) was performed on 157 samples (Table 1). Samples were reacted with 15 ml of a 2 mol L⁻¹ HCl solution for 2 h, or with 10 mL of a 6 mol L⁻¹ HCl solution for 48 h when bulk mineralogy showed evidence of dolomite. The δ^{13} C isotope analysis was performed in duplicate on a Vario Micro Cube elemental analyser coupled in continuous flow mode to an isotope ratio mass spectrometer (IsoPrime, Elementar, Hanau, Germany) at the Biogéosciences Laboratory (GISMO platform, Université Bourgogne Europe). Certified USGS40 (with $\delta^{13}C_{org} = -26.39\%$) and caffeine IAEA-600 ($\delta^{13}C_{org} = -27.77\%$) international reference materials were used for calibration. Carbon isotope composition is expressed in delta notation and reported in permil (%) relative to the Vienna Pee Dee Belemnite (VPDB) standard. External reproducibility based on duplicate analyses of samples is better than $\pm 0.2\%$ (1 σ).

Palynological analyses were carried out on six samples from Isles-les-Meldeuses and Ussy-sur-Marne, among which only one contained a quantitatively rich palynomorph association. Palynomorphs were concentrated using standard palynological techniques (i.e. Erdtman, 1960; Roche *et al.*, 2008) with the methodology described in Iakovleva *et al.* (2021).

RESULTS

Facies and associated depositional environments

Facies recognition based on field (Fig. 3A to C), macroscopic and microscopic observations (Figs 4 and 5), combined with previous descriptions for the Le Tillet core (Cavelier, 1968), and for the Ussy-sur-Marne core and the Isles-les-Meldeuses outcrop (Briais, 2015), resulted in 11 facies (F1 to F11) grouped into four facies associations (FA1 to FA4), interpreted in terms of depositional environments (Table 2).

The first facies association (FA1) includes facies F1, F2a and F2b (Table 2). F1 is composed

of medium-to-coarse sand and mud, with 3D megaripples, metre-scale erosion channels, cross-bedding stratification, tangential oblique lamination, ripple cross-bedding and mud drapes with bioclasts in the bottomsets (Table 2). Rare bivalves and gastropods are present, as well as bioturbations such as Ophiomorpha, especially at the top of the megaripples. F2a is composed of fine to coarse glauconitic sand and mud with bioclasts, and is marked by ripple cross-bedding and mud drapes with a micritic matrix and bioclasts (Table 2). F2b is composed of coarse sand to conglomerate with gravels and is marked by 3D megaripples with tangential oblique laminations and channelized erosional surfaces (Table 2; Fig. 3C). Both facies F2a and F2b contain reworked material (e.g. carbonate clasts, clavev pebbles and bioclasts, mainly from the underlying MCF).

FA1 is interpreted as a siliciclastic-dominated estuary (Van Wagoner et al., 1990; Cattaneo & Steel, 2003; Boyd et al., 2006; Zecchin & Catuneanu, 2013). Tidal influence is indicated by the presence of 3D megaripples, cross-bedding and mud drapes. The transition from coarse sand to conglomerate with 3D megaripples in Isles-les-Meldeuses (F2b) to fine-to-coarse glauconitic sand with ripple cross-bedding and mud drapes in Le Tillet (F2a) indicates a deepening pattern. Along with this lateral variation, the presence of reworked material in both F2a and F2b is interpreted as a transgressive lag (Van Wagoner et al., 1990; Cattaneo & Steel, 2003; Zecchin & Catuneanu, 2013). FA1 is assigned to the SaA unit (Figs 6 and 7).

The second facies association (FA2) includes facies F3, F4a, F4b and F5, mainly composed of packstone and grainstone rich in bioclasts (Fig. 4A and B). The main difference between these facies is their bioclastic content and size (Table 2), with serpulids and oysters in F3, foraminifera in both F4a and F4b (e.g. miliolids, *Nummulites, Orbitolites complanatus*), but smaller and more peloidal in F4b than in F4a (Table 2). F5 is enriched in sand but still contains foraminifera and bioclasts.

The packstone-to-grainstone texture, the presence of cross-bedding stratification and the fragmentation of most biotic components suggest an agitated environment. Among these biotic components, the presence of shallow benthic foraminifera (e.g. *Nummulites*, orbitoids, and locally abundant miliolids), along with *characeae* and molluscs (e.g. oysters), suggests rather shallow marine conditions in facies association FA2.

1868 J. Talon et al.

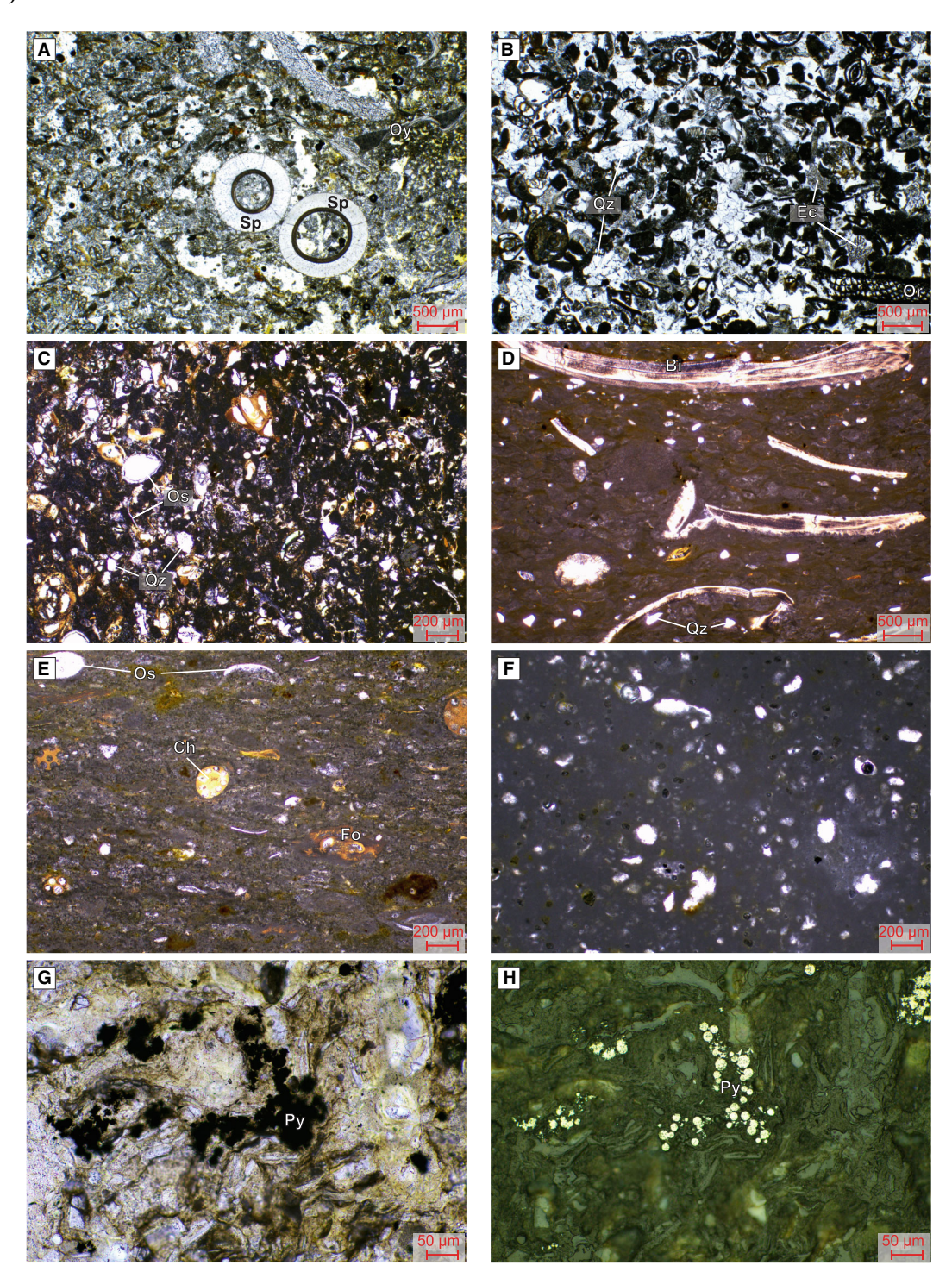


Fig. 4. Microfacies described in Table 2. (A) Facies F3 (Sample Us 47.20): Packstone with serpulids (Sp), Oyster fragments (Oy) and bioclasts; (B) Facies F4 (Sample LT 58.00): Grainstone with foraminifera such as miliolids and Orbitolites complanatus (Or), bioclasts (e.g. echinoids (Ec)) and quartz grains (Qz); (C) Facies F6a (Sample LT 56.10): Bioclastic micropackstone with foraminifera, ostracods (Os), peloids and quartz grains (Qz); (D) Facies F7 (Sample SMx 08): Floatstone with bivalves (Bi), foraminifera and quartz grains (Qz) embedded in a micritic matrix with granulation and circumgranular cracks; (E) Facies F8 (Sample SMx 09): Laminated wackestone with foraminifera (Fo), ostracods (Os) and Characeae (Ch); (F) Facies F9a (Sample SMx 21): Dolomicritic wackestone with dissolved or recrystallized bioclasts; (G) and (H) Clayey facies F10 (Sample Us 32.60), pyrite (Py) under polarized light (G) and reflected light (H) highlighting framboidal morphology of pyrite.

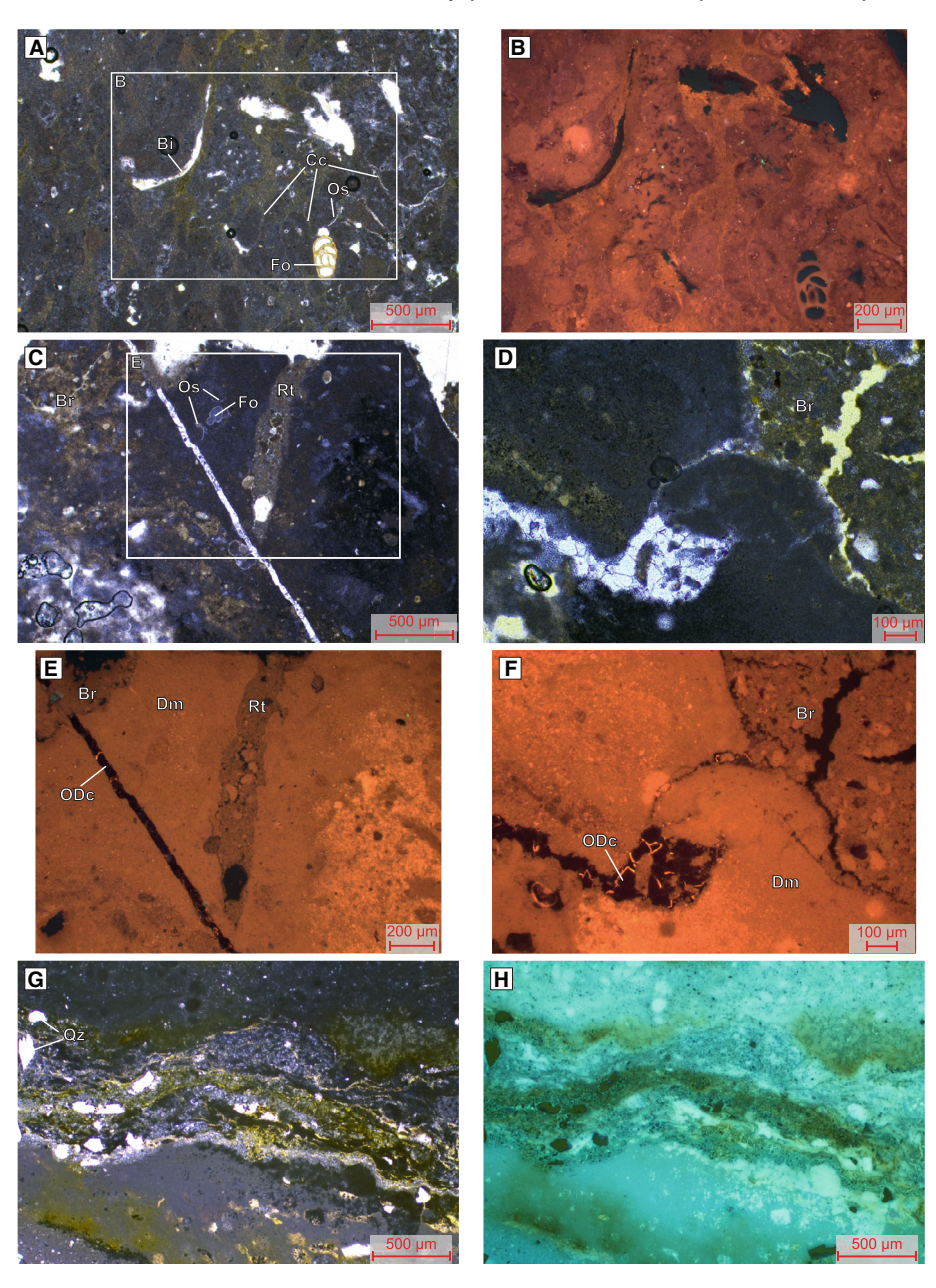


Fig. 5. Pedogenetic and microbial features described in Table 2. (A) Granular matrix and circumgranular cracks (Cc) within facies F6a (Sample LT 52.90), with bioclasts such as foraminifera (Fo), bivalves (Bi) and ostracods (Os); (B) detail of A, using cathodoluminescence, highlighting granulation and cracks; (C) dolomicritic facies F9a (Sample Us 26.10) with root traces (Rt), brecciation (Br) and cracks filled by calcite. Rare foraminifera (Fo) and ostracods (Os); (D) dolomicritic facies F9a (Sample Us 26.10) with cracks filled by calcite and brecciation (Br); (E) detail of C using cathodoluminescence, showing the dark and bright orange luminescence of calcite in the fractures (ODc) and the dull orange luminescence of the dolomicrite (Dm). Bright orange on the right is an artefact; (F) cathodoluminescence observation of D, showing bright orange and dark luminescence of calcite (ODc) in the cracks and the dull orange luminescence of the dolomicrite (Dm). Bright orange in the matrix is an artefact; (G) dark micritic laminae and peloids showing crenulation within the dolomicritic facies associated with quartz (Qz; F9c; Sample LT 48.25); (H) epifluorescence observation of G with mixed UV light and blue light (respectively, 75% and 25%), highlighting the microbial crenulation.

Table 2. Facies associations, facies description and interpretation in terms of sedimentary processes and depositional environments.

Facies		:			Sedimentary structures and	Pedogenetic and		Depositional
Association	Facies	Core/Outcrop	Lithology	Components	bedding	diagenetic features	Sedimentary processes	environment
	FI	Outcrop (IM) and core (LT, Us)	Medium to coarse sand and mud.	Rare bivalves and gastropods, bioturbations (e.g. Ophiomorpha). Subangular to rounded quartz grains.	3D megaripples (metre scale) with bioturbations at the top and tangential oblique laminations; ripple cross-bedding and mud drapes with bioclasts in the bottomsets, meter-scale erosion channel	Automorphic quartz cement around some grains.	Tidal process	
FAI	F2a	Core (LT)	Fine to coarse glauconitic sand and mud, with bioclasts and reworked carbonate clasts.	Bioclasts (foraminifera (e.g. rotalids), articulated to disarticulated ostracods, echinoids, gastropods, bivalves, Characeae, algae, bryozoans). Angular quartz grains and glauconitic prains	Ripple cross-bedding and mud drapes with micritic matrix and bioclasts.	Characeae are micritised.	Tidal process and transgressive lag	Siliciclastic-dominated estuary
	F2b	Outcrop (IM)	Coarse sand to conglomerate, with gravel, clayey pebbles and reworked carbonate clasts.	Bioturbations and rare bivalves.	3D megaripples (metre scale) with tangential oblique laminations, channelised erosional surfaces (Fig. 3C).			
	F3	Core (Us)	Packstone to grainstone with serpulids and oysters. (Fig. 4A)	Millimetric, mostly unbroken serpulids, bivalves (cm-disarticulated oyster, broken or not), gastropod moulds, bioclasts (e.g. foraminifera, echinoids, ostracods), and peloids. Angular to sub-rounded quartz grains (~100 µm) and glauconitic grains.	Possible cross-bedding.	Micritic to microsparitic cement, foraminifera can be filled by glauconite. Bioclasts are often micritised or recrystalised.	Relatively high energy	
FA2	F4a	Core (LT, Us) and outcrop (SMx)	Packstone to grainstone with foraminifera and bioclasts. (Fig. 4B)	Foraminifera (rotalids, miliolids, Nummulites, Orbitolites complanatus,), bioclasts (e.g. echinoids, algae, bivalves, gastropods). Angular to sub-rounded quartz grains		Micritic to microsparitic matrix, syntaxial cement around echinoids, foraminifera are often micritised.	Relatively high energy	Marine-influenced
	F4b	Core (LT, Us) and outcrop (SMx)	Packstone to grainstone with foraminifera, bioclasts, and quartz grains.	Like Fq., but with peloids, and smaller foraminifera and bioclasts. Abundant, mostly angular, quartz grains (~100 µm).	Possible laminated organisation.	More pronounced micritisation of the foraminifera.	Relatively high energy	bay
	F5	Outerop (SMx)	Fine, well-sorted, greenish glauconitic sand.	Foraminifera and bioclasts (e.g. Characeae, echinoids, bivalves, gastropods) preferentially filling bioturbations. Angular to sub-rounded, well-sorted quartz grains (50-100 µm); abundant, very fine to fine (~10 µm) glauconitic particles. Opaque lithic fragments	Intense bioturbation filled in by a whitish bioclastic packstone to grainstone.	Locally indurated with microsparitic cement. Partially micritised foraminifera.	Relatively high energy	

1365391, 2025, 6, Downbladed from https://onlinelibrary.wiley.com/doi/10.1111/sed.07024 by Cochane France, Wiley Online Library on [17/9/2025]. See the Terms and Conditions (https://onlinelibrary.viley.com/terms-and-conditions) on Wiley Online Library for rules of use; OA articles are governed by the applicable Creative Commons License

Table 2. (continued)

Facies		9			Sedimentary structures and	Pedogenetic and	;	Depositional
Association	Facies	Core/Outerop	Lithology	Components	bedding	diagenetic features	Sedimentary processes	environment
		Core (LT, Us), Outcrop (IM)	Wackestone to (micro)packstone with bioclasts and peloids. (Fig. 4C)	Bioclasts, including foraminifera (mostly miliolids), articulated to disarticulated ostracods, bivalve fragments, gastropods (often unbroken) up to mm-size, abundant micritic		Micritic to microsparitic cement. Bioclasts can be micritised or recrystallised and bivalve fragments can be dissolved.	Moderate energy, emersion phases and moderate to relatively intense pedogenesis	
	F6a			peloids. Possible plant fragments, intraclasts, and microbial laminae (crenulation and highly variable porosity). Angular to sub-rounded (~50 µm to ~150 µm) quartz grains and altered		Granular matrix, circumgranular cracks (Fig. 5A-B), highly variable porosity, brecciation and possible root traces.		
FA3	F6b	Core (LT)	Dolomitic packstone with micritic peloids.	glauconitic grains. Moulds of dissolved bioclasts (e.g. foraminifera, echinoids, bivalves, possible ostracods). Angular quartz grains (50-150 µm).		Dissolution. Micritic to microsparitic dolomitic cement with mostly anhedral dolomite crystals, up to 15 µm, recrystalising peloids and some bioclasts. Possible granulation.	Slightly higher energy, storm wash-over (?), mixing zone (?)	Coastal bay
	F7	Outerop (SMx)	Floatstone beds (cm to dm) rich in flattened gastropods and bivalves, passing upwards to mudstone with rare foraminifera and ostracods. (Fig. 4D)	Millimetric to centimetric, almost complete gastropods (e.g. <i>Potamides lapidorum</i>), disarticulated and fragmented bivalve shells. Some isolated shell fragments, foraminifera (mostly miliolids). Smaller and fewer shells upwards. Microbial crenulations. Angular to sub-rounded quartz grains (~50-100 um).	Erosive base, shelly concentration (coquina) and desiccation cracks.	Micritic matrix with granulation, brecciation, circumgranular cracks and desiccation cracks filled in by a sparitic cement or silicifications.	Storm wash-over, fluctuating salinity, emersion phases and relatively intense pedogenesis	
	<u>&</u>	Outcrop (SMx)	Laminated calcitic wackestone, with ostracods and characeae. (Fig. 4E)	Mostly unbroken Characeae, articulated and disarticulated ostracods, miloids, small bivalve fragments, peloids. Possible microbial laminations. Angular to sub-rounded quartz grains.	Bioclasts organised in horizontal laminations.	Ostracods are sometimes recrystallised and miliolids are often micritised.	Decantation	
FA4	F9a	Core (Us)	Homogeneous dolomicritic mudstone to wackestone, with rare bioclasts. (Fig. 4F)	Bioclasts are mostly foraminifera and ostracods, rarely bivalves and gastropods (often only moulds). Wackestone to packstone intraclasts with poorly preserved foraminifera, echinoids, and ostracods. Sub-rounded to angular quartz grains (~50-100 µm).		Dissolved and recrystallised bioclasts. Dolomitisation. Granulation, brecciation, root traces, calcite with dark or orange eathodoluminescence filling cracks (Fig. 5C to F).	Decantation, emersion phases and intense pedogenesis	Restricted coastal bay to sabkha

Table 2. (continued)

Facies					Sedimentary structures and	Pedogenetic and		Depositional
Association	Facies	Core/Outcrop	Lithology	Components	bedding	diagenetic features	Sedimentary processes	environment
	F9b	Core (LT, Us) and outcrop (SMx, IM)	Homogeneous dolomicritic mudstone.	No fauna. Probable microbial crenulations. Presence of quartz grains.	Small vugs (probably dissolved bioclasts). Possible horizontal laminations.	Dissolution and dolomitisation.	Decantation	
	F9c	Core (L.T)	Dolomicritic mudstone.	Micritic peloids and microbial crenulations with quartz grains (Fig. 5G-H).		Dolomitisation. Silica microprecipitations (~100 µm). Granulation.	Decantation, possible emersion, and moderate pedogenesis	
	F10	Core (Us) and outcrop (SMx, IM)	Centimetric to decimetric clay horizons.	Rare ostracods, foraminifera, bivalves and gastropod fragments. Quantitatively rich dinocyst assemblage with Glaphyrocysta microfenestrata, Enneadocysta pectiniformis, E. robusta, Thalassiphora fenestrata etc., dominated by Homotryblium abbreviatum (~45%) and very common Spiniferites, Areoligara- and Thalassiphora-groups. Derrital quartz grains and rare glauconitic grains.		Micrometric dolomite crystals and framboidal pyrite (Fig. 4G-H).	Decantation	
	F11	Core (Us) and outcrop (SMx, IM)	Gypsum pseudomorphs in calcite or quartz in a dolomicritic matrix.	No fauna. Centimetric to decimetric disorganised aggregates (efflorescences) of small (up to ~5 mm) lenticular crystals. Isolated crystals within a dolomicritic matrix.		Gypsum pseudomorphs in calcite or quartz. Dolomitisation.	Evaporitic conditions	

This facies association is interpreted as a marine-influenced bay (Reynaud *et al.*, 2012; Briard *et al.*, 2020) and is assigned to units CD and CMO (Figs 6 and 7).

The third facies association (FA3) includes facies F6 to F8 (Table 2). 'Crenulated micritic laminae' (F8 to F9) and 'clotted' fabrics (F6) are often observed in FA3. Facies F6a has a wackestone-to-micropackstone texture, with bioclasts and abundant peloids (Fig. 4C). Bioclasts include foraminifera (mostly miliolids), ostracods (sometimes articulated) and often unbroken gastropods up to millimetre-size. Peloids are individual or fused in clusters and organized in laminae. They can be distinguished from wellrounded faecal pellets by their smaller size and diffuse contour (Flügel, 2004). These peloids are ordered in mesoclots (Kennard & James, 1986). Their association with dense micritic laminae supports a microbial origin (Vennin et al., 2019). This facies also contains plant fragments and intraclasts. F6a often presents a granular matrix and circumgranular cracks (Fig. 5A and B), with highly variable porosity as well as brecciation and possible root traces (Table 2). Facies F6b is a dolomitic packstone with micritic peloids and moulds of dissolved bioclasts (e.g. foraminifera, bivalves and possible ostracods). This facies is by a micritic-to-microsparitic dolomitized cement mainly composed of anhedral dolomite crystals (up to 15 µm), replacing peloids and bioclasts (Table 2). Facies F7 is a very localized facies corresponding to floatstone beds of flattened, almost complete gastropods (e.g. Potalapidorum), mides and fragmented, disarticulated bivalve shells (Fig. 4D). Facies F7 has an erosive base, evolving upwards into mudstone with rare gastropods, bivalves, foraminifera and ostracods. Continuous stacked or coalescent thin micritic laminae are observed, sometimes alternating with laminated peloids. F7 is affected by granulation, brecciation, circumgranular cracks and desiccation cracks filled with calcite sparite or silica. Facies F8, also local, is a laminated wackestone composed of planar laminations of unbroken Characeae, ostracods (sometimes articulated), miliolids and small bivalve fragments (Fig. 4E). It also contains diffuse peloids organized in a clotted structure (10 to 100 µm), with dense crenulated micritic laminae.

Moderate energy is indicated by the wackestone-to-micropackstone texture, the abundant micrite and micritic peloids, as well as the presence of articulated ostracods and unbroken gastropods (F6a). The presence of a granular matrix, granular cracks, brecciation and root traces suggests emersion associated with pedogenesis. The packstone texture suggests slightly higher hydrodynamic conditions, while the replacement of peloids and recrystallization of bioclasts by small anhedral dolomite crystals (F6b) could indicate dolomitization processes in the mixing zone (Petrash et al., 2021). The floatstone texture, the erosive base, the shelly concentration and the thinning-upwards organization (F7) suggest storm wash-over deposits, while the accumulation of Potamides lapidorum suggests fluctuating salinities. Emersion phases and relatively intense pedogenesis are marked granulation, brecciation, circumgranular cracks and desiccation cracks filled by sparitic cement or silicifications. The combination of micrite, micritic peloids, crenulated micritic laminae, unbroken Characeae and articulated ostracods (F8) suggests very low energy and probably decantation processes. Microbial mats, composed of crenulated micritic laminae and peloid clusters, ubiquitously form in the intertidal zone, associated with dolomite forming as a primary precipitate (Bouton et al., 2016; DiLoreto et al., 2019). The micritic clotted texture aligns with observations from other studies (Arenas & Pomar, 2010; Hips et al., 2015). These studies interpret such features as evidence of microbially mediated calcium carbonate precipitation. The clotted texture observed in this study is thought to result from organically mediated calcification processes, leading to the formation of clots and/or the cementation of peloids. Facies association FA3, combining these three facies, reflects a shallow environment with moderate energy and sporadic emersion, here interpreted as a coastal bay (Reynaud et al., 2012; Briard et al., 2020).

The last facies association (FA4) includes facies F9 to F11 (Table 2). Facies F9 corresponds mainly to relatively homogeneous dolomicritic mudstones and has been subdivided based on fossil content, as well as pedogenetic and diagenetic features. F9a contains rare bioclasts (mostly foraminifera and ostracods, moulds of gastropods and bivalves) wackestone-to-packstone intraclasts (Table 2). Bioclasts are often dissolved or recrystallized (Fig. 4F), and this facies is affected by granulation, root traces and calcite-filled cracks sealed by brecciation (Fig. 5C and D). The calcite filling the cracks is non-luminescent under CL (Fig. 5E and F). Facies F9b presents small vugs, probably

13653091, 2025, 6, Downloaded from https://onlinelibrary.wiley.com/doi/10.1111/sed.70024 by Cochrane France, Wiley Online Library on [17/09/2025]. See the Terms and Conditions (https://onlinelibrary.wiley.com/terms

and-conditions) on Wiley Online Library for rules of use; OA articles are governed by the applicable Creative Commons License

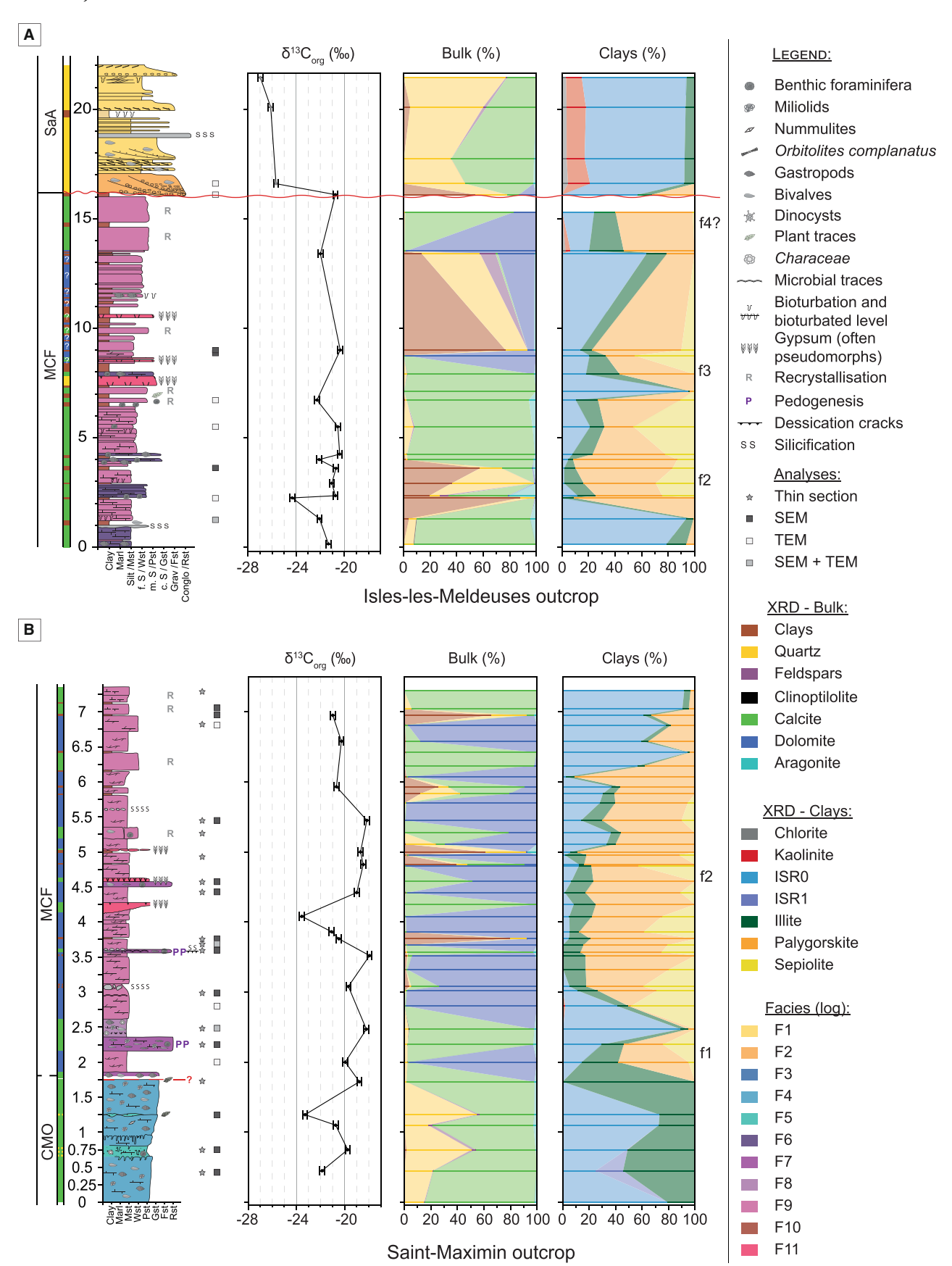
Fig. 6. Sedimentological log with organic carbon isotopes ($\delta^{13}C_{org}$), bulk and clay mineralogy (XRD) of the cores Le Tillet (A) and Ussy-sur-Marne (B). Biostratigraphy and lithostratigraphy are based on descriptions by Cavelier (1968) for the Le Tillet core and Briais (2015) for the Ussy-sur-Marne core. Depth in metres. CD: 'Calcaire à Ditrupa strangulata' unit; CMO: 'Calcaire à Milioles et Orbitolites complanatus' unit, MCF: 'Marnes et Caillasses' Formation, SaA: 'Sables d'Auvers' unit, SaB: 'Sables de Beauchamp' unit. Colours within the log correspond to facies defined in Table 2. Labels (f1 to f4) correspond to identified fibrous clay mineralogical events.

corresponding to dissolved bioclasts bird-eyes, microbial crenulation and planar lamination (Table 2). Facies F9c contains diffuse micritic peloids organized in clusters, silica micro-precipitations and crenulated and irregular micritic laminae encompassing quartz grains (Table 2; Fig. 5G and H). It is also affected by granulation. Facies F10 consists of centimetricto-decimetric clay horizons with rare ostracods, foraminifera and bivalve and gastropod fragments (Table 2). Micrometric dolomite crystals and framboidal pyrites are observed in this facies (Fig. 4G and H). In facies F10, one sample from Ussy-sur-Marne vielded a quantitatively rich palynological assemblage, composed almost entirely (~99%) of dinoflagellate cysts (dinocvsts) with single bissacate and angiosperm pollen grains. The dinoflagellate cyst assemblage contains ~35 species, among which Glaphyrocysta microfenestrata, G. intricata, Enneadocysta pectiniformis, E. robusta and Thalassiphora fenestrate, possibly suggesting a latest Lutetianearly Bartonian age for the deposits (Powell, 1992). This assemblage is dominated by Homotryblium-group (mostly Homotryblium abbreviatum, ~45%), while Spiniferites ramosus (~14%), Areoligera-group (~14%) and Thalassiphora pelagica (~9%) are very common. Facies F11 consists of gypsum pseudomorphs in calcite or quartz, embedded inside a dolomicritic matrix (Table 2).

In facies association FA4, the dolomicritic texture and clavev horizons of facies F9 and F10 indicate very low energy and most likely decantation processes, while the gypsum pseudomorphs of facies F11 indicate evaporitic conditions. The dinocyst assemblage may indicate restricted marine to open marine inner neritic settings. The high abundance of representatives of the dinocyst genus Homotryblium is considered to reflect warm and dry intervals with reduced run-off and strong evaporation (Brinkhuis, 1994; Sluijs et al., 2005). Homotryblium abbreviatum forms almost half of the dinocyst assemblage, suggesting increased

salinity in a nearshore setting. Microbial mats are often formed in shallow-water evaporitic environments, as shown by their presence in many modern hypersaline lagoons (Gerdes & Krumbein, 1987), and marine intertidal and supratidal areas (Lokier, 2013; Court et al., 2017; Carmeille et al., 2018; Manaa & Aref, 2022). Granulation, root traces and calcite-filled cracks sealed by brecciation indicate emersion and intense pedogenesis, particularly in facies F9. In this facies, the calcite filling is non-luminescent under CL (Fig. 5E and F), indicating oxidizing conditions, while bright luminescent orange growth zonation suggests rapidly fluctuating redox conditions. The framboidal pyrites in facies F10 probably reflect sulphate-reducing bacterial activity (Machel, 2001: et al., 2004; Wen et al., 2020; Li et al., 2022). Facies association FA4 is interpreted as a restricted coastal bay (Reynaud et al., 2012; Briard et al., 2020), which can reach sabkha-like conditions. FA3 and FA4 are assigned to the MCF (Figs 3A and B, 6 and 7), with a regional emersion surface at the top (SB in Fig. 2; e.g. Pomerol, 1989; Briais, 2015; Marie, 2023; Moreau, 2023; Moreau et al., 2024), which is locally karstified (Fig. 3C).

The facies in these four facies associations vary both laterally and vertically along a NW-SE transect, from Le Tillet to Ussy-sur-Marne (Fig. 8). The erosional surface between the carbonate system (corresponding to the MCF: FA2-FA4) and the siliciclastic sediments (corresponding to units SaA and SaB: FA1) is assigned to a sequence boundary (SB in Fig. 2) recognizable at basin scale (Haq et al., 1988; Briais, 2015; Marie, 2023; Moreau et al., 2024). Based on chemostratigraphy (see Organic carbon isotopes), a 2 to 5% negative $\delta^{13}C_{org}$ excursion is used as a datum to correlate the four sections. The lateral and vertical facies variations along this transect record a transition from a marineinfluenced bay (FA2) to a more coastal bay (FA3), with laterally restricted environments (FA4) becoming dominant upwards, especially



13653091, 2025, 6, Downloaded from https://onlinelibrary.wiley.com/doi/10.1111/sed.70024 by Cochrane France, Wiley Online Library on [17/09/2025]. See the Terms and Conditions (https://onlinelibrary.wiley.com/derns

-and-conditions) on Wiley Online Library for rules of use; OA articles are governed by the applicable Creative Commons License

13653091, 2025, 6, Downloaded from https://onlinelibrary.wiley.com/doi/10.1111/sed.70024 by Cochrane France, Wiley Online Library on [17/09/2025]. See the Terms and Conditions (https://onlinelibrary.wiley.com/terms-and-conditions) on Wiley Online Library for rules of use; OA articles are governed by the applicable Cerative Commons License

Fig. 7. Sedimentological log with organic carbon isotopes ($\delta^{13}C_{org}$), bulk and clay mineralogy (XRD) of the outcrops Isles-les-Meldeuses (A) and Saint-Maximin (B). Lithostratigraphy is based on field descriptions by Briais (2015) for the Isles-les-Meldeuses outcrop. Elevation in metres. CMO: 'Calcaire à Milioles et *Orbitolites complanatus*' unit, MCF: 'Marnes et Caillasses' Formation, SA: 'Sables d'Auvers' unit. Colour within the log corresponds to facies defined in Table 2. Labels (f1 to f4) correspond to identified fibrous clay mineralogical events.

towards the south-east. The erosion observed at the top of the MCF seems to be more pronounced towards the north-west (see also Marie, 2023).

Dolomite characterization

The magnesium-rich carbonates observed in the coastal bay (FA3) and restricted coastal bay (FA4) environments are composed of micrometric grains (Fig. 9A to D); they present the characteristic XRD ordering reflections (101), (015) and (021) of dolomite (Fig. 9E; Bradley et al., 1953; Gregg et al., 2015). The lower intensity of the (015) ordering reflection compared to the (110) reflection suggests some cation disorder in the dolomite in these two facies associations (Goldsmith & Graf, 1958; Gregg et al., 2015). The Ca/Mg ratio of dolomite can be estimated using Lumsden (1979) equation's, based on the slight shift of the (104) reflection towards lower 2θ values, indicating between 51 and 56 mol% CaCO3 in FA3 dolomite and between 52 and 57 mol% CaCO3 in FA4 dolomite. In the coastal bay (FA3), dolomite microcrystals mimetically replace earlier grains, cements and organic remains (Fig. 9A). They present a dark to non-luminescent core, alongside concentric and sectoral zoning under cathodoluminescence (Fig. 9B). Dolomite crystals are even smaller in sediments from the restricted environment (FA4; Fig. 9C and D), resulting in a homogeneous dull orange luminescence. In these dolomite crystals, any growth or sectoral zoning is barely visible, although some crystals appear to have cores darker than their rims (Fig. 9C). In dolomite crystals, Mg²⁺ substitution by Mn²⁺ results in a red colour under cathodoluminescence, while Ca²⁺ substitution by Mn²⁺, which is not common, results in a green to yellowish colour (El Ali et al., 1993; Richter et al., 2003). These substitutions are also observed in cathodoluminescence emission spectra, with a distinctive emission peak at \sim 650 nm for $\rm Mg^{2+}$ substitution and at \sim 575 nm for $\rm Ca^{2+}$ substitution. Cathodoluminescence spectral analysis of the studied dolomites (Fig. 9F) shows a broad peak resulting from the overlap of the two aforementioned peaks of roughly similar intensity, leading to yellow-greenish to orange emission colour under cathodoluminescence, making it difficult to differentiate from calcite without spectral analysis (Fig. 9B and C) and suggesting a high substitution of Ca²⁺ by Mn²⁺. The SEM observations (Fig. 9G and H) confirm the micrometric size (ranging from <1 to 10 µm), the presence of both rhombohedral and anhedral dolomite microcrystals, and reveal the presence of a hollow core in most crystals, which could explain the non-luminescent character of the crystal cores under cathodoluminescence.

Clay mineralogy

In the clay fraction (<2 µm) of the CMO unit ('Calcaire Grossier' Formation), clay minerals are dominated by R0-type mixed-layer illite/smectite (ISR0, referred to as 'smectite' hereafter; avg = 67%) and illite (avg = 31%; Figs 6 and 7; Table S1). By contrast, in the clay fraction of the MCF, clay minerals are generally dominated by fibrous clays: palygorskite (avg = 43%, max = 98%) and sepiolite (avg = 7%, max = 48%). Smectite is also present in the MCF (avg = 39%) and even dominant in the Le Tillet core (avg = 64%). Fibrous clay-dominated events are recognized throughout the MCF, interbedded in the smectite-rich background sedimentation (f1 to f4 in Figs 6 and 7). In the clay fraction of the SaA and SaB units, clay minerals are characterized mainly by smectite and also by illite, while kaolinite occurs sporadically (from 5% to 17%; Figs 6 and 7; Table S1).

Smectite-rich intervals in the MCF, identified by XRD (Fig. 10A), show a diffuse cloudy shape in TEM images (Fig. 10B) while palygorskite-rich and sepiolite-rich intervals, identified by XRD (Fig. 10A), display the characteristic fibre-like habitus in TEM images, variable in length, yet relatively short (Fig. 10C). Higher resolution TEM images reveal the presence of rods (formed by two or more laths), aggregated into bundles (Fig. 10D), corresponding to the fibres observed in SEM images (García-Romero & Suárez, 2013). In SEM images, the typical platy or flaky structure of

NW-SE correlation transect of the four studied sections (Le Tillet core, Saint-Maximin outcrop, Isles-les-Meldeuses outcrop and Ussy-sur-Marne core). The carbon isotope negative shift to -24% is used as an isochron for the MCF. CD, 'Calcaire à Ditrupa strangulata' unit; CMO, 'Calcaire à Milioles et Orbitolites complanatus' unit; MCF, 'Marnes et Caillasses' Formation; SaA, 'Sables d'Auvers' unit; SaB, 'Sables de Beauchamp' unit. Fig. 8.

13653991, 2025, 6, Downloaded from https://onlinelibrary.wiley.com/doi/10.1111/sed.70024 by Cochrane France, Wiley Online Library on [17/09/2025]. See the Terms and Conditions (https://onlinelibrary.wiley.com/terms-and-conditions) on Wiley Online Library for rules of use; OA articles are governed by the applicable Cerative Commons Licensea

detrital smectite (Iacoviello et al., 2012) is observed, but sometimes with small fibres emerging from the flakes (Fig. 11A). No features such as hairy shape, rose shape or honeycomb structure which are generally interpreted as evidence of neoformed smectites (Fesharaki et al., 2007; Iacoviello et al., 2012) were observed, indicating that mostly detrital smectites are present. Fibrous clays display large flakes with a wavy organization around detrital grains in low-resolution SEM images (Fig. 11B). Higher resolution images clearly highlight the common fibrous habitus (Fig. 11C) and a clayey matrix mainly composed of entangled small fibres (Fig. 11D), closely associated with dolomite (Fig. 11E). The EDS analyses reveal the systematic presence of magnesium alongside potassium, calcium and iron within the smectite particles, while small proportions of calcium, potassium and iron are still present within the palygorskite particles (Fig. 11F).

Organic carbon isotopes

Organic carbon isotope ($\delta^{13}C_{org}$) results are presented for each section, from the most distal to the most proximal. For Le Tillet, $\delta^{13}C_{org}$ values vary between -22.3% and -21% within the CMO unit and between -23.3% and -19.2% with an average value of -20.9% in the MCF (Fig. 6A). The most negative value (-23.3%) is observed at a depth of 49 m. The interval between 42 m and 38.5 m is characterized by scattered values (ranging from -26% to -19.1%; Table S2), corresponding to reworked material. In the SaA and SaB units, negative values are recorded, with an average value of -27%. For Saint-Maximin, $\delta^{13}C_{org}$ values are quite variable within the CMO unit (ranging from -23.3% to $-18.78\%_{o}),$ with an average value of $-20.9\%_{o}$ (Fig. 7B). In the MCF, $\delta^{13}C_{org}$ values vary between -23.6% and -18%, with an average value of -19.8%, and the most negative value (-23.6%); Table S2) is found at the base of the formation (at ~4 m). For Isles-les-Meldeuses, δ¹³C_{org} values within the MCF have an average value of -21.5% and are marked by a negative peak (at ~ 2.30 m) with a value of -24.3%(Fig. 7A; Table S2). In the SaA unit, values decrease to an average of -26.3%. For Ussy-sur-Marne (Fig. 6B), the CD and CMO units are marked by contrasted $\delta^{13}C_{org}$ values (ranging from $-24.13\%_{00}$ to $-18.1\%_{0}$). In the MCF, $\delta^{13}C_{org}$ values vary between -24.6% and -19.5%, with an average value of -21.4%, and the most negative value (-24.6%) is found at the base of the

formation (at a depth of \sim 36 m; Table S2). In the SaA unit, negative values are recorded, with an average value of -26%.

Even though background $\delta^{13}C_{org}$ values differ, a negative excursion with an amplitude of 2 to 5‰ is observed towards the base of the MCF for all four sections. This negative excursion is considered an isochron for the transect in Fig. 8. The unconformity at the top of the MCF corresponds to a strong negative shift (5 to 7‰ amplitude) in the three sections where it is observed (Le Tillet, Isles-les-Meldeuses and Ussy-sur-Marne).

DISCUSSION

Depositional environments and magnesian minerals

From the marine environment of the 'Calcaire Grossier' Formation to the more restricted coastal bay environments of the MCF, the studied succession is characterized by a shallowing-upwards trend topped by a locally karstified and erosive surface, interpreted as a maximum regressive surface (Fig. 8; Haq et al., 1988; Briais, 2015; Marie, 2023; Moreau et al., 2024). This surface is overlain by a transgressive lag (F2a and b) initiating a deepening trend and the development of a siliciclastic estuarine system (FA1; Fig. 8). A lateral continuity between a marine-influenced bay and a coastal bay, as proposed in Fig. 12, is suggested by (i) episodic marine incursions (i.e. 'Falun de Foulangues' unit; F.F in Fig. 2) in the NW of the studied area (Cavelier & Le Calvez, 1965; Briais, 2015; Gély, 2016); (ii) the presence of similar facies to FA2 (foraminifera-rich deposits including abundant Nummulites) in the Channel strait (Fig. 1A; Auffret et al., 1975), probably contemporaneous with FA3 identified in the MCF, as indicated by the occurrence of *Alveolina* elongata (i.e. SBZ17); (iii) poorly preserved foraminifera in the more restricted facies (F9 and F10). Such lateral facies variation in the Paris Basin has also been proposed by Broekman (1984) and Fontes & Toulemont (1987). In the studied sections, the transition between the marineinfluenced and the restricted coastal bay seems abrupt (Fig. 8). A sequence boundary between the marine 'Calcaire Grossier' Formation and the more restricted MCF cannot be ruled out, as suggested by Brachert et al. (2023). Within the MCF, based on the correlation between the four studied sites (Fig. 8), the coastal bay (FA3) becomes

© 2025 The Author(s). Sedimentology published by John Wiley & Sons Ltd on behalf of International Association of Sedimentologists, Sedimentology, 72, 1860–1898

1363991, 2025, 6, Downloaded from https://onlineibrary.wiley.com/doi/10.1111/sed.07024 by Cochanne France, Wiley Online Library on [1709/2025]. See the Terms and Conditions (https://onlineibrary.wiley.com/rems-ad-conditions) on Wiley Online Library for rules of use; OA articles are governed by the applicable Creative Commons Licensee

Fig. 9. Dolomite from the coastal bay (FA3) and restricted coastal bay (FA4) environments. (A) Dolomitized packstone to grainstone (facies F6b, FA3, sample LT 49.00), bioclasts are either dissolved or recrystallized by small dolomite crystals; (B) detail of A, under cathodoluminescence, highlighting small, mostly anhedral dolomite crystals (<10 µm), exhibiting dull orange-brown luminescence, with some more greenish or reddish shades in sectoral zoning and darker luminescent cores; (C) homogeneous dolomicritic facies (F9a, FA4, sample LT 52.00) under cathodoluminescence, highlighting micrometric dolomite crystals, exhibiting a dull to orange-brown occasionally greenish-vellow luminescence, sometimes with a darker luminescent core. The darker corner (bottom-left) corresponds to a non-luminescent calcite crystal filling a pore. Green dots are artefacts from the abrasive powder; (D) detail of C under polarized light, highlighting micrometric, anhedral to rhombohedral dolomicrite grains; (E) Xray diffraction patterns for the two dolomite samples shown in A-D, displaying detail between 20° and 55° 2 θ and calibrated on the (slight) (101) quartz reflection. Dolomite reflection (d), calcite (c) and quartz (q), dolomite ordering reflections (101), (015) and (021) are indicated with an asterisk. Mol% CaCO₃ is calculated using Lumsden's (1979) equation based on position of the (104) reflection of dolomite (LT49.00: d(104d) = 2.900 Å and LT52.00: d(104d) = 2.897 Å); (F) cathodoluminescence spectra for the two dolomite samples shown in A-D, compared with calcite (UWC3) and dolomite (UW6220) standards from the University of Wisconsin - Madison (Cui et al., 2022); (G) SEM observation of facies F9b (FA4, sample SMx 29) showing mostly anhedral, micrometric dolomite crystals with a hollow core. Note the presence of palygorskite fibres around some crystals; (H) SEM observation of micrometric dolomite crystals embedded in a clayey (palygorskite) matrix (facies F10, FA4, sample SMx 17). Some dolomicritic crystals present a hollow core.

laterally more restricted towards the south-east, with localized marine incursions corresponding either to small channels (F6) or higher energy episodes, such as storm wash-over deposits (F7; Fig. 12). In the restricted coastal bay (FA4), the presence of significant evaporitic sabkha-like deposits is indicated by the large gypsum lenses around Paris (Facies F11), often tens of metres thick (Toulemont, 1987) and also by microbial mats (F9).

The three shallow-water carbonate environments (FA2 to FA4) are characterized by distinctive mineralogical associations (Fig. 12). The relatively high-energy marine-influenced bay (FA2) is dominated by calcite, and the very low clay content (<1%) is composed of smectite and illite assemblages. Dolomite and Mg-fibrous clays (palygorskite and sepiolite) appear in the transitional coastal bay (FA3), suggesting more evaporitic conditions. These conditions become dominant in the restricted coastal bay (FA4), where the clay content rises to a maximum of 88% (16% on average), reflecting higher decantation processes. In FA4, palygorskite (up to 98% in some samples) and sepiolite (up to 48% in some samples) are dominant, representing an average of 55% in the clay mineralogy. A noticeable decrease in smectite content within the clay fraction is observed as the environment becomes more restricted (Fig. 12). This progressive decline suggests either that the main source of smectites is the open marine domain or that smectite destabilization in restricted environments results in the formation of other clay minerals (Eberl et al., 1987; Deconinck et al., 1988; Inglès &

Anadón, 1991). At that time, smectite and illite were the dominant clay minerals in the marine domain of the Hampshire and North Sea basins (Huggett & Knox, 2006), again suggesting a detrital origin for smectite from the open marine domain. In contrast, Mg-fibrous clays are only dominant in the restricted coastal bay, where they generally form a dense matrix of short entangled fibres (Fig. 11), often in close association with small dolomite crystals (Figs 9H and 11E). The clear edges of palygorskite in TEM images (Fig. 10B to D) and the presence of iron within palygorskite fibres (Fig. 11F) also suggest an *in situ* formation process (Del Buey *et al.*, 2025).

Formation of fibrous clays and dolomite in a coastal bay environment

Early dolomite formation in the Paris Basin
The co-occurrence of fibrous clays and dolomite
observed in the Eocene deposits of the Paris
Basin has been described in similar restricted
coastal settings and/or evaporitic environments
(Isphording, 1973; Inglès & Anadón, 1991; Del
Buey et al., 2018; Perri et al., 2018; Kirkham &
Huggett, 2020), raising questions about the conditions and mechanisms regulating their
formation.

The two morphologies of dolomite observed in the Paris Basin coastal bay suggest two processes of formation (Fig. 13). The dolomite identified in the restricted coastal bay deposits (FA4) is characterized by micrometric, anhedral to rhombohedral crystals with a hollow core (Fig. 9), features commonly associated with primary dolomite formation influenced by microbial activity in evaporitic environments (Pineda etal.. 2021: Sánchez-Román et al., 2023). This dolomite also presents a slight cation disorder and Ca-enrichment, with unusual greenish-vellow to orange cathodoluminescence, reflecting high substitution of Ca²⁺ by Mn²⁺ (Fig. 9), typical of syn-sedimentary or early diagenetic dolomite formed under evaporitic conditions (Gillhaus etal.. 2010: et al., 2022). The presence of clotted and laminated microbial structures (in FA4) in the MCF. in association with dolomite, suggests the potential role of microorganisms in syngenetic to early diagenetic dolomite formation (Fig. 5G and H). Microbial activity and its associated organomineral substances (extracellular polymeric substances—EPS), as well as poorly crystallized Mg-Si phases, can fix and facilitate the dehydration of cations and act as nucleation sites, thus promoting early dolomite formation (Fig. 13; Bontognali et al., 2010; Krause et al., 2012; Zhang et al., 2012a,b; Pace et al., 2016; Petrash et al., 2017; Perri et al., 2018; Guo et al., 2023a, b; Sánchez-Román et al., 2025). These microbial mechanisms require a sustained high pH (above 8) to precipitate the Si-Mg phases and fix cations (Pace et al., 2016; Petrash et al., 2017; del Buev et al., 2023; Mather et al., 2023). Indeed, dolomite precipitation associated with microbial activity generally occurs at pH above 7.5 (Warthmann et al., 2000; van Lith et al., 2003; Wacey et al., 2007; Sánchez-Román et al., 2011).

In coastal bay deposits (FA3), dolomite crystals are generally coarser than in the restricted coastal bay deposits (FA4), but still under 10 µm (Fig. 9). These crystals are also anhedral to rhombohedral, with a similar slight cation disorder and Ca-enrichment, as well as unusual greenish-yellow to orange cathodoluminescence (Fig. 9). Replacing previous grains and cements, these larger crystals display sectoral zoning under cathodoluminescence (Fig. 9), suggesting relatively rapid crystal growth under disequilibrium conditions (Reeder & Prosky, 1986). Replacement of a carbonate precursor, promoted by increasing temperature and alkalinity in addition to increasing Ca and Mg concentrations and Mg/Ca ratio, is a commonly inferred nearsurface dolomite formation process (Machel, 2004; McKenzie & Vasconcelos, 2009; Gregg et al., 2015). These early diagenetic dolomites are promoted under evaporitic conditions (Folk & Land, 1975; McKenzie, 1981; Illing & Taylor, 1993; Zentmyer et al., 2011). The so-called

'dolomites', later qualified as very highmagnesium calcite (VHMC) or proto-dolomite (Gregg et al., 2015; Kaczmarek et al., 2017), directly precipitated in evaporitic conditions, and were perhaps microbially influenced (Vasconcelos et al., 1995; Bontognali et al., 2012; Sá nchez-Román et al., 2025). They could then become precursors and transform into more ordered dolomite through early diagenetic ageing processes (Fig. 13; Vasconcelos & McKenzie, 1997; Petrash et al., 2021; Neuhuber et al., 2024). This dolomite is therefore interpreted as being primarily related to early dolomitization processes of a pre-existing carbonate phase, such as calcite, aragonite, proto-dolomite or VHMC. There is no evidence in the Paris Basin coastal bay environments of secondary late diagenetic dolomite, another potential pathway for dolomite formation (Fig. 13). Two primary or early diagenetic dolomite formation mechanisms are therefore retained: (i) the influence of microbial activity in the restricted coastal bay (FA4); (ii) rapid recrystallization from a carbonate or VHMC precursor in the more open coastal bay (FA3).

Fibrous clay formation in the Paris Basin

In the Lutetian-Bartonian coastal bay deposits of the Paris Basin (FA3-4), TEM and SEM images show relatively short palygorskite fibres (no more than a few micrometres; Figs 10, 11 and 14) suggesting rapid nucleation under high ionic saturation (García-Romero & Suárez, 2013). The SEM images of palygorskite fibres emerging from Mg-smectites, and dense, flaky palygorskite entanglements strongly suggest the transformation from smectite to palvgorskite, with palygorskite retaining some of the morphology of smectite (Figs 11, 14A and B). The size of the initial smectite particles might control to some extent the size of the palygorskite fibres formed. The systematic presence of iron and potassium in both Mg-smectite and palygorskite in the EDS spectra (Fig. 11E) further suggests a precursor mineral enriched in K and Fe, such as detrital Al-Fe-smectite. The observed Mg-smectite would thus result from magnesium incorporation into the initial detrital Al-Fe-smectite, as previously described in similar environments (Trauth, 1977; Weaver & Beck, 1977). Subsequently, increased magnesium occupancy within Mg-smectite octahedral sites would induce lattice strains, resulting in inversion from a sheet structure (e.g. smectite) to a chain-like structure (e.g. palygorskite), as

13653091, 2025, 6, Downloaded from https://onlinelibrary.wiley.com/doi/10.1111/sed.70024 by Cochrane France, Wiley Online Library on [17/09/2025]. See the Terms and Conditions (https://onlinelibrary.wiley.com/terms

-and-conditions) on Wiley Online Library for rules of use; OA articles are governed by the applicable Creative Commons License

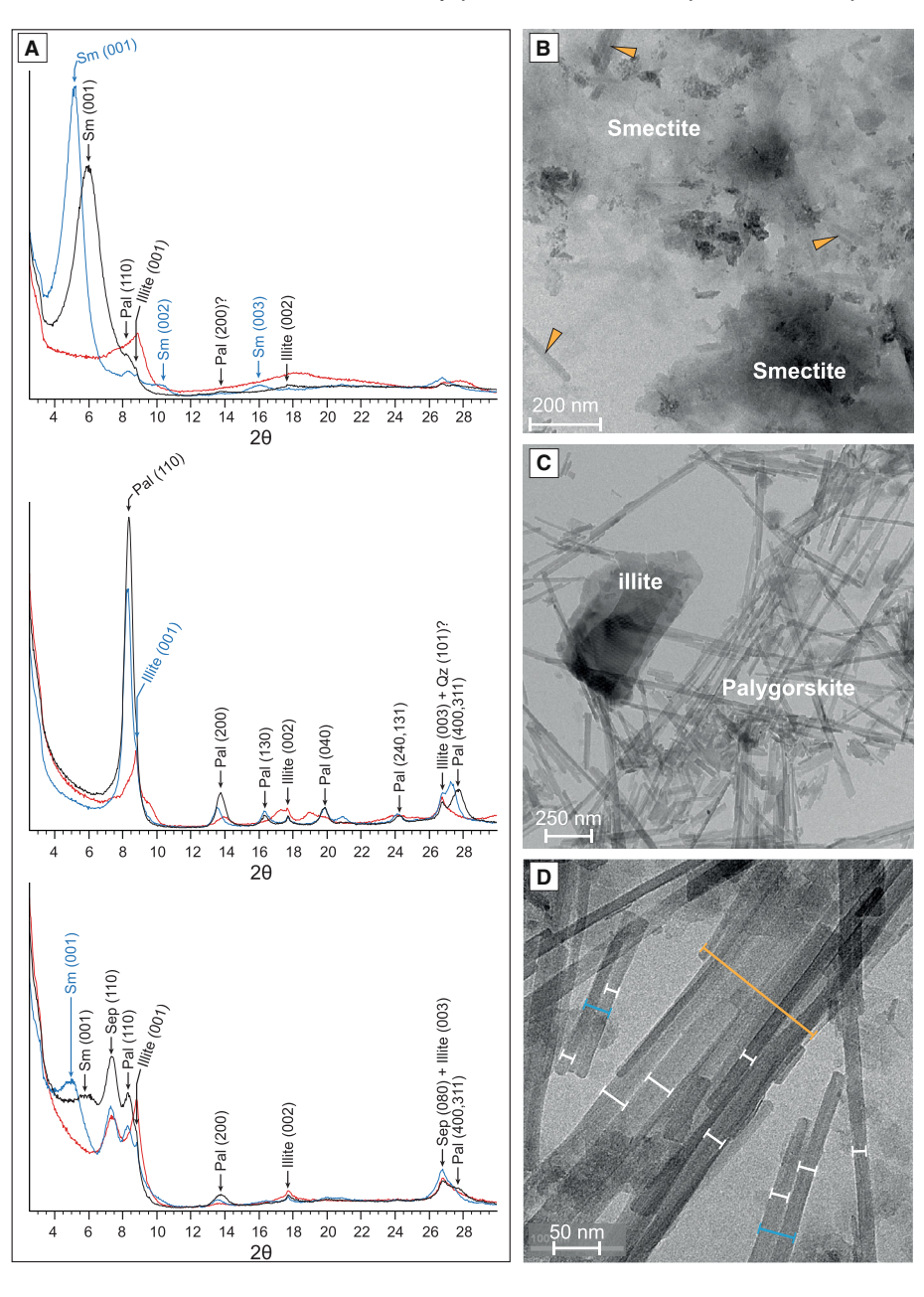


Fig. 10. X-ray diffraction patterns (A) and TEM images (B–D) of selected clay samples. (A) Representative X-ray diffraction patterns of oriented mounts from key clay samples, showing the three treatments (air-dried in black, ethylene-glycol saturation in blue and heating at 490°C for 2 h in red). From top to bottom: Smectite-rich sample with minor palygorskite and illite (Sample Us 32.60), Palygorskite-rich sample with minor illite (Sample Us 35.40) and fibrous clay-rich sample also containing smectite and illite (Sample IM 10). Sm: smectite, Sep: sepiolite, Pal: palygorskite and Qz: quartz. (B) Smectite-rich sample, with orange arrows indicating short palygorskite fibres (Sample SMx 09); (C) Palygorskite fibres and detrital illite crystal in a palygorskite-dominated sample (Sample IM 04); (D) Detail of palygorskite fibres, showing laths in white, rods in blue and bundles in orange (Sample LT 38.55).

suggested by Weaver & Pollard (1973) and Chen *et al.* (2004). Detrital smectites could provide the aluminium necessary for palygorskite formation (Trauth, 1977; Weaver & Beck, 1977; Xie *et al.*, 2013), while direct precipitation of

sepiolite from solution would occur afterwards, when aluminium activity is low (Fig. 13). After investigating Priabonian and Oligocene deposits (Paris Basin, SE France, and Morocco), Trauth (1977) proposed that the

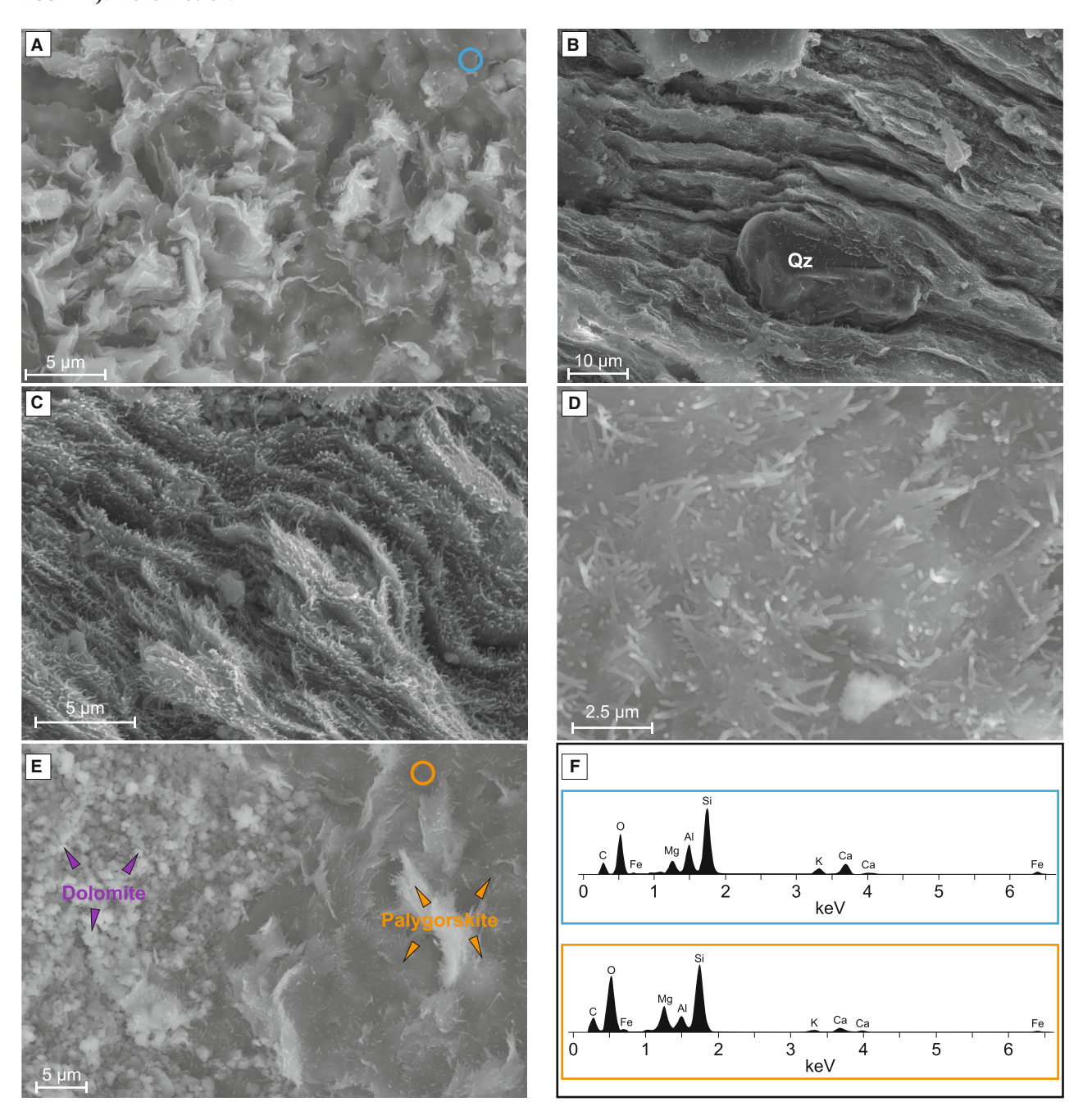


Fig. 11. SEM images of selected clay samples. (A) Detrital smectite, with fibre-like structures emerging from the flakes (Sample Us 32.60); (B) detrital quartz grain within palygorskite laminae (Sample IM 18); (C) detail of sample IM 18 showing wavy palygorskite laminae, highlighting the fibrous habitus; (D) palygorskite matrix made of entangled fibres (Sample Us 36.60); (E) microcrystalline dolomite and palygorskite fibres (Sample Us 36.60); (F) EDS spectra for smectite, framed in blue (blue circle in image A), and palygorskite, framed in orange (orange circle in image E).

transformation of Mg-smectite into palygorskite is also controlled by the ratio between silica in solution and magnesium available for clay formation (i.e. Si/Mg ratio). This author suggested that Mg-smectite undergoes conversion into palygorskite under a high Si/Mg ratio, then sepiolite precipitates from the solution. Conversely, a low Si/Mg ratio favours Al-saponite,

1365391, 2025, 6, Downloaded from https://onlinelibrary.wiley.com/doi/10.1111/sed.70024 by Cochrane France, Wiley Online Library on [17/09/2025]. See the Terms and Conditions (https://onlinelibrary.wiley.com/terms-and-conditions) on Wiley Online Library or rules of use; OA articles are governed by the applicable Cerative Commons License

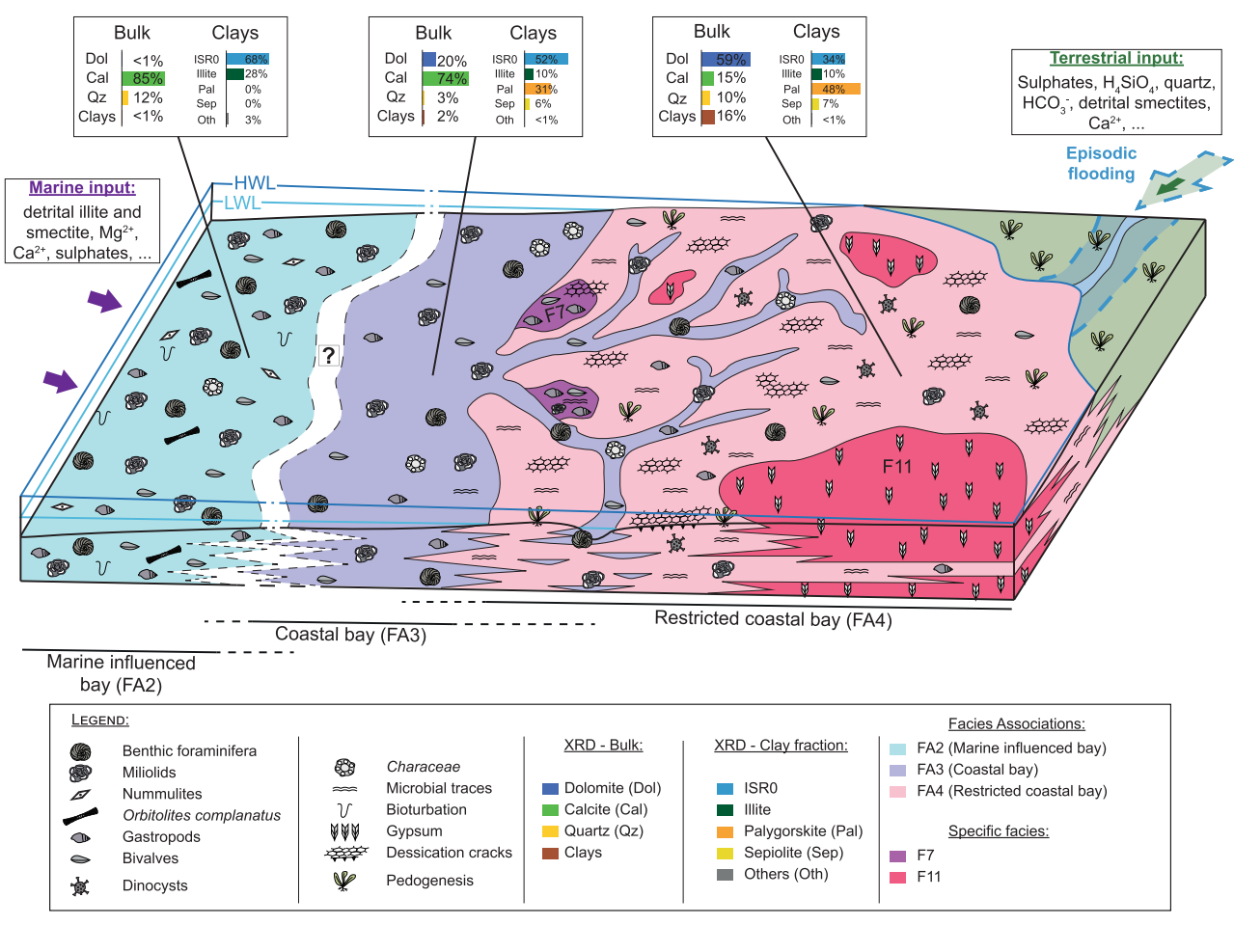


Fig. 12. Depositional model proposed for the Paris Basin during the late Lutetian—early Bartonian, with average bulk and clay mineralogies, representative of the marine-influenced bay and the coastal bay. HWL, high water level; LWL, low water level. The separation and question mark represent the uncertainty regarding the lateral facies variation between FA2 and FA3 (see text for a detailed discussion).

followed by Mg-saponite formation, and finally stevensite precipitation from the solution (Fig. 13). In addition to high silica and magnesium activity, fibrous clay formation requires a pH between 8 and 9.5, and relatively high aluminium activity for palygorskite (Fig. 13; Birsoy, 2002; Galán & Pozo, 2011; Guggenheim & Krekeler, 2011).

The SEM images of palygorskite fibres developing inside dissolved dolomite and growing out of dolomite crystals (Fig. 14C to E) also suggest a process of dolomite dissolution, promoting palygorskite formation within the restricted coastal bay environment (FA4). Previous studies have hypothesized that the input of slightly acidic meteoric water would lead to the dissolution of poorly ordered dolomite, releasing

hydrogenocarbonate and magnesium ions, thus increasing pH and magnesium activity, promoting palygorskite formation (Fig. 13; Inglès & Anadón, 1991; Ryan *et al.*, 2019).

Here, the presence of Mg-smectite and the subsequent formation of palygorskite is interpreted as mainly resulting from the transformation of detrital Al-Fe-smectite, which probably entered the Paris Basin coastal bay through both marine and terrestrial inputs (Fig. 12). Direct precipitation from solution is frequently proposed for fibrous clay formation during pedogenesis (Singer & Norrish, 1974; Galán & Pozo, 2011). Such a mechanism cannot be ruled out in the Paris Basin as emersion and pedogenesis features are clearly identified in the restricted coastal bay deposits (FA4; Fig. 5A to

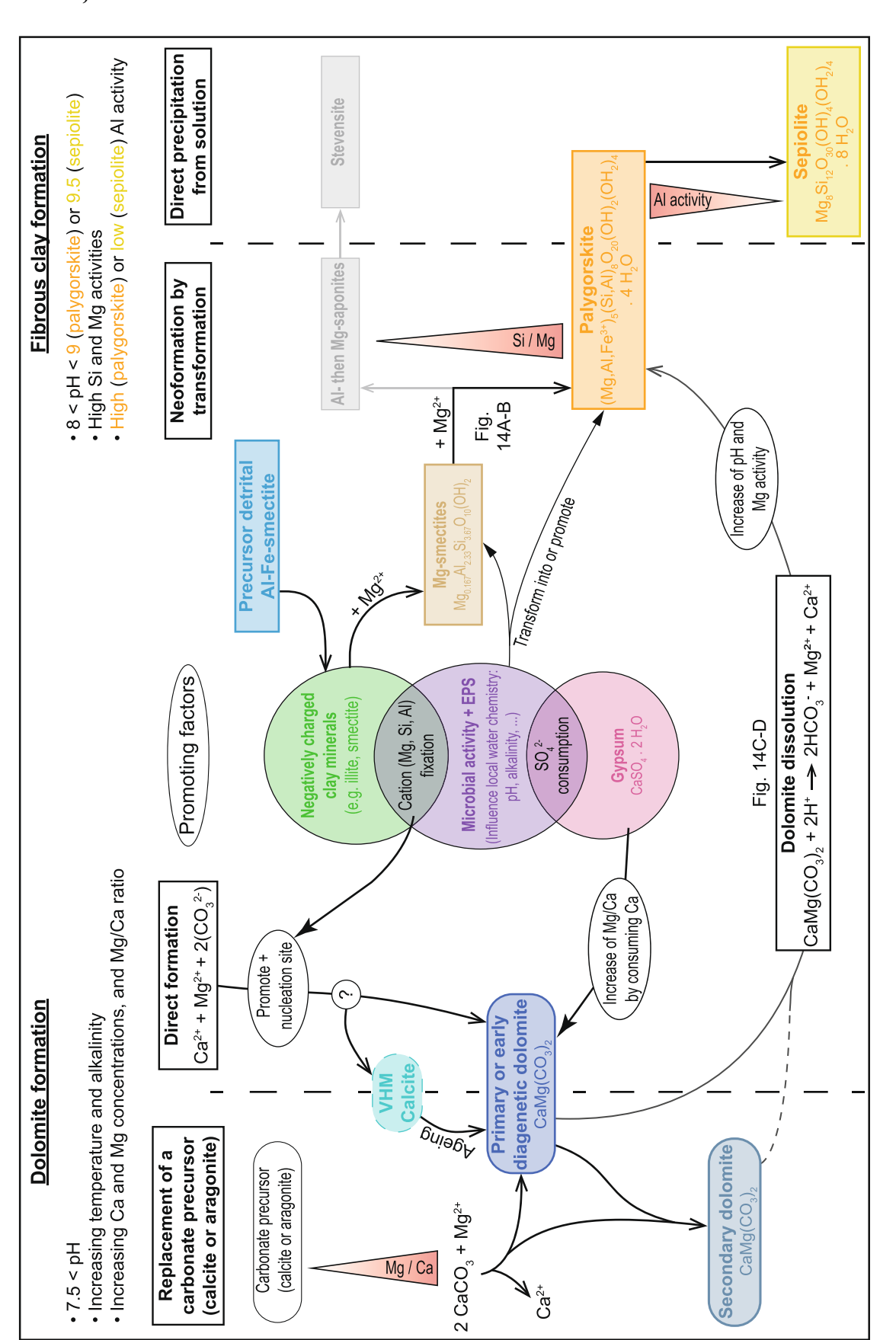


Fig. 13. A comprehensive model for the concomitant early formation of palygorskite and dolomite in coastal marine environments: mechanisms and favourable conditions. Formulas for palygorskite and sepiolite after Pozo & Calvo (2018), Mg-smectite formula after Birsoy (2002). Favourable conditions for fibrous clay formation after Birsoy (2002), Galán & Pozo (2011) and Guggenheim & Krekeler (2011); factors enhancing dolomitization rates after Gregg et al. (2015) and Pace et al. (2016). Mechanisms are detailed in the text and are compared to the data obtained in the Paris Basin.

1365391, 2025, 6, Downloaded from https://onlinelibrary.wiley.com/doi/10.1111/sed.70024 by Cochrane France, Wiley Online Library on [17/09/2025]. See the Terms and Conditions (https://onlinelibrary.wiley.com/terms-and-conditions) on Wiley Online Library for rules of use; OA articles are governed by the applicable Creative Commons Licenses

13653091, 2025, 6, Downloaded from https://onlinelibrary.wiley.com/doi/10.1111/sed.70024 by Cochrane France, Wiley Online Library on [17/09/2025]. See the Terms and Conditions (https://onlinelibrary.wiley.com/terms-and-conditions) on Wiley Online Library for rules of use; OA articles are governed by the applicable Cerative Commons License

Fig. 14. SEM data illustrating the mechanisms described in Fig. 13. (A) Fibre-like structures emerging from Mg-smectite flakes (Sample Us 32.60) representing the transformation from a sheet to a chain-like structure due to magnesium incorporation; (B) entangled palygorskite fibres reminiscent of the typical flaky smectite morphology (Sample Us 36.60). This could represent an advanced transformation stage of a smectite flake into palygorskite; (C) small palygorskite fibres growing in place of a dissolved dolomite crystal (Sample SMx 16); (D) palygorskite fibre growing on a dissolving anhedral dolomite crystal (around 2 μ m) with a hollow core (Sample SMx 21); (E) EDS spectra of the palygorskite fibre (orange) growing from the dolomite crystal (purple) in image D.

F), but SEM observations mainly highlight processes of transformation from detrital smectite and dolomite dissolution for palygorskite formation.

A model reconciling the concomitant early formation of dolomite and fibrous clays To overcome competition for magnesium, the concomitant formation of palygorskite and primary or early diagenetic dolomite requires favourable factors, shown in this study to be present in the late Lutetian—early Bartonian coastal bay of the Paris Basin (Figs 12 and 13).

Microbial activity (microbial mats and EPS) could act as a template and ionic reservoir, promoting both dolomite and Mg-clay formation, yet requiring slightly different pH conditions (Del Buey *et al.*, 2018, 2021; Perri *et al.*, 2018;

1888 J. Talon et al.

Sánchez-Román *et al.*, 2023, 2025; Cupertino *et al.*, 2024). These highly variable pH conditions may have been influenced through biological and physical processes such as those found in modern marine environments:

- 1 Uptake of inorganic carbon by phytoplankton during photosynthesis may increase pH, while release of CO₂ through respiration processes will decrease pH, resulting in large seasonal or even daily pH variations in coastal environments (Raven, 1991; Wallace et al., 2014; Baumann & Smith, 2018; Raven et al., 2020).
- 2 Sulphate-reducing bacteria (SRB)-related processes occur within a wide range of pH values (Widdel, 1988; Hao et al., 1996; Koschorreck, 2008). The presence of SRB in the restricted coastal bay of the Paris Basin is evidenced by framboidal pyrite (Fig. 4G to H) and also by sulphur isotopes (Fontes & Toulemont, 1987). Microbial sulphate reduction and the associated anaerobic degradation of organic matter also contribute to dolomite formation at low temperatures, locally increasing alkalinity and producing EPS (Vasconcelos & McKenzie, 1997; Sánchez-Román et al., 2009b; Petrash et al., 2017; Yao et al., 2024). Indeed, by regulating the pCO2 and alkalinity, methanogenesis and anaerobic methane oxidation control the formation of dolomite in organic-rich marine sediments (Moore et al., 2004).
- 3 Occasional freshwater inputs into a hypersaline restricted environment (Krumgalz, 1980). Previous studies of the MCF have inferred the impact of freshwater inputs on salinity and ionic concentrations (Fontes *et al.*, 1970; Renard, 1972; Fontes & Toulemont, 1987), coherent with a schizohaline environment (Folk & Siedlecka, 1974).

Such highly fluctuating and dynamic hydrogeochemical conditions might also provoke shifts in microbial communities and in EPS composition and production (DiLoreto et al., 2019, 2021), facilitating dolomite (Deelman, 1999; McCormack et al., 2024) as well as fibrous clay formation.

The circulation of slightly acidic meteoric water during emersion phases would have lowered the pH, impeding fibrous clay formation. This effect would have been counterbalanced by the dissolution of newly formed poorly ordered dolomite, increasing pH as well as magnesium activity, therefore promoting palygorskite formation once again (Fig. 13).

Interestingly, negatively charged clay minerals such as illite or smectite, similar to microbial communities and associated EPS, may facilitate dolomite formation (Fig. 13; Liu et al., 2019; Wen et al., 2020; Molnár et al., 2021). Transforming detrital Al-Fe-smectite into Mg-smectite could therefore act as a precursor for palygorskite and also promote dolomite formation. The direct precipitation of Mg-smectite and dolomite is further favoured by high silica activity (Fang & Xu, 2022; Hobbs et al., 2024). Observations of occasional silicification as nodules or thin lavers interspersed within dolomite in the MCF (Fig. 7) provide evidence of high silica activity. Such silicifications prove the high availability of silica to increase the Si/Mg ratio, favouring the transformation of detrital smectite into palygorskite instead of saponite. This Si/Mg ratio is also enhanced by dolomite formation (Fig. 13).

Gypsum precipitation, induced by the evaporitic conditions prevailing in the Paris Basin during the late Lutetian–early Bartonian, would have further increased the Mg/Ca ratio and Mg²⁺ availability, thus promoting both the formation of dolomite (Zentmyer *et al.*, 2011) and fibrous clays (Fig. 13).

In summary, simultaneous primary or early diagenetic formation of Mg-fibrous clays and poorly ordered dolomite is favoured by factors such as (i) microbial activity, (ii) detrital alumina—silicate inputs, (iii) early carbonate precursors, (iv) dissolved silica availability and (v) gypsum precipitation. These factors, highly dependent on environmental changes in schizohaline settings, would induce slight variations in physico-chemical conditions (e.g. pH, Mg/Ca, Si/Mg) and biological activity, and may thus explain the intricate Mg-rich minerals observed in the late Lutetian—early Bartonian deposits of the Paris Basin, as summarized in the comprehensive model proposed in Fig. 13.

Forcing mechanisms (climate and palaeogeography) on clay sedimentation

In the Paris Basin, a fibrous clay-rich episode is recorded within the MCF, along the 65 km long transect studied here (Fig. 15). Assigned to the Lutetian–Bartonian transition from benthic foraminifera (SBZ15-17), nannofossil (NP16) and dinocyst assemblages, this fibrous clay-rich episode is the earliest one identified in the Cenozoic of the NW European domain (Pomerol, 1967; Trauth et al., 1968). Interrupting

the smectite-dominated sedimentation of the Eocene, this episode can be divided into four fibrous clay-rich events (f1 to f4), despite some discrepancies in the evolution of the clay content (Fig. 15). The f2 event is concomitant with the most negative $\delta^{13}C_{\rm org}$ values ($\sim\!-24\%$) in the MCF. In the Le Tillet core, this negative organic carbon isotope excursion immediately precedes the level where SBZ17 is identified, marking the beginning of the Bartonian stage (Serra-Kiel et al., 1998). Based on this biostratigraphic constraint, and in agreement with isotopic trends along the transect, this negative organic carbon isotope excursion is here assigned to the Late Lutetian Thermal Maximum (LLTM; Fig. 15).

The transient LLTM (~30 kyr), corresponding to the last Palaeogene hyperthermal event within a global long-term cooling trend, has been dated at 41.52 Ma in deep-marine records (Fig. 15; Speijer et al., 2020; Westerhold et al., 2020). The LLTM is marked by negative isotope excursions measured on benthic foraminifera ($\sim 0.8\%$ δ^{13} C and $\sim 0.5\%$ δ^{18} O), interpreted as a ~2°C warming of deep seawater (Edgar et al., 2007; Westerhold et al., 2018a). This event coincides with the highest insolation values of the last 45 Myr (Westerhold & Röhl, 2013; Intxauspe-Zubiaurre et al., 2018; Westerhold et al., 2018a). Such hyperthermal climate conditions would have led to extreme seasonal contrast, with prolonged dry seasons and occasional rainfall and run-off episodes on land (Intxauspe-Zubiaurre et al., 2018; Westerhold et al., 2018a). Short run-off episodes inland would thus have punctuated the generally arid conditions, while evaporative conditions probably persisted in coastal settings. Semi-arid to arid conditions are confirmed by the predominant palygorskite and sepiolite preserved in the Lutetian-Bartonian coastal bay deposits of the Paris Basin, as these fibrous clay minerals are unstable under a wet climate (Chamley, 1989; Galán & Pozo, 2011). Brief freshwater inputs inferred from oxygen, sulphur and strontium isotopes (Fontes et al., 1970; Renard, 1972; Fontes & Toulemont, 1987) highlight the extremely variable salinity conditions recorded in the MCF. Such conditions are confirmed by euryhaline biotic assemblages mainly composed of Cerithiidae, Sphaenia, Corbula and Potamididae (Abrard, 1925: Gély, 1996). Extreme seasonal variability induced by the LLTM event could thus have enhanced evaporation in the Paris Basin bay, while increased rainfall on land may have caused periodic flooding (Fig. 12). These climate

conditions would have led to a schizohaline environment particularly favourable to the formation of fibrous clays and dolomite (Folk & Land, 1975; Weaver & Beck, 1977), that is confirmed by higher proportions of palygorskite and sepiolite (fibrous clay event f2) during the LLTM in Saint-Maximin, Isles-les-Meldeuses and Ussysur-Marne (Fig. 15), according to the position of the LLTM based on carbon isotopes and biostratigraphic data.

In addition to climate influence, palaeogeographical changes could explain the clay mineralogy variability (smectite versus fibrous clays) recorded in the MCF. Smectite content is higher in the Le Tillet core, particularly in the 'Falun de Foulangues' unit (SBZ17, Le Tillet core, Fig. 15), which is interpreted as a marine incursion in the NW Paris Basin (Cavelier & Le Calvez, 1965; Briais, 2015; Gély, 2016). Smectite is also predominantly recorded in the more open settings of the Hampshire and North Sea basins (Huggett & Knox, 2006). Based on the palaeogeographical reconstruction of the NW European domain (Fig. 1), a detrital origin is proposed for the smectite observed in the NW Paris Basin, possibly related to marine incursions (Fig. 12). Alternatively, fluvial inputs from the eastern Vosges and NE Ardenno-Rhenish Massifs (Blondeau, 1965; Sissingh, 1998, 2003) may have provided detrital smectite in more proximal settings towards the SE (i.e. Ussy-sur-Marne core), particularly during episodic flooding (Fig. 12). The progressive emersion of the Artois High during the late Lutetian–early Bartonian may have resulted from long-wavelength Pyrenean tectonic deformation (Briais, 2015). This change in palaeogeography gradually restricted the Paris Basin by its isolation from the Belgian and North Sea basins (Fig. 1A; Pomerol, 1978; Cavelier & Pomerol, 1979; Gély, 1996; King, 2006). The resulting flat coastal bay, favouring an increase in ion concentration, is expected to have promoted magnesian mineral formation.

During the late Lutetian—early Bartonian, both climate and palaeogeographical changes could have favoured the formation of Mg-fibrous clays and dolomite in the Paris Basin, but disentangling these two forcing mechanisms remains difficult. Supporting the climate hypothesis are the palygorskite and sepiolite identified in the upper Lutetian lacustrine deposits and soils around the Paris Basin (Thiry, 1989); in late Lutetian—Bartonian deposits in the shallow carbonate gulf of the Campbon Basin, France (Fig. 1A; Esteoule-Choux, 1970, 1984); in the

Fig. 15. Clay mineralogy and carbon isotope ($\delta^{13}C_{org}$) correlation between the studied sections, and proposed correlation with global-scale data. The carbon - 24‰ is used as an isochron. The $\delta^{^{18}}O_{\mathrm{benthic}}$ (purple) and $\delta^{^{13}}C_{\mathrm{benthic}}$ (black) data from Westerhold et al. (2020) are presented for comparison. The proposed correlation between the isochron and the LLTM event, marked by more negative values, is outlined in green. Shading represents warmer (red) to colder (blue) temperature trends, based on δ^{18} O_{benthic} data. Clay mineralogical events are reported, highlighting up to four fibrous clay events (f1 to f4) within the MCF. The chronostratigraphic framework is from the GTS 2020 (Speijer *et al.*, 2020). CD, 'Calcaire à *Ditrupa strangulata'* unit; 'Calcaire à Milioles et Orbitolites complanatus' unit; LLTM, Late Lutetian Thermal Maximum; MCF, 'Marnes et Caillasses' Formation; SaA, 'Sables warmer (red) to colder (blue) temperature trends, based on $\delta^{18} O_{\mathrm{benthic}}$ d'Auvers' unit; SaB, 'Sables de Beauchamp' unit. isotope negative shift to \sim

13653991, 2025, 6, Downloaded from https://onlinelibrary.wiley.com/doi/10.1111/sed.70024 by Cochrane France, Wiley Online Library on [17/09/2025]. See the Terms and Conditions (https://onlinelibrary.wiley.com/terms-and-conditions) on Wiley Online Library for rules of use; OA articles are governed by the applicable Cerative Commons Licensea

upper Lutetian lacustrine-to-palustrine deposits in NE and SE France (Valleron et al., 1983); in the Lutetian evaporitic lagoonal deposits in southern Italy (Cavalcante et al., 2011); and in Ypresian-to-Bartonian alluvial-to-lagoonal deposits in Spain (Inglès & Anadón, 1991). In similar climate conditions, however, the middle Eocene estuarine bay deposits of SE England (Isle of Wight; Fig. 1A), with high fluvial influx (Plint, 1983; Clark et al., 2022), mainly record smectite and illite, with kaolinite content decreasing from east to west (Huggett & Knox, 2006). The Lutetian-Bartonian siliciclastic marine deposits in Belgium also record smectite and illite, with minor kaolinite and chlorite (Mercier-Castiaux et al., 1988). The low ion concentrations and predominance of detrital influxes in these more open depositional environments result in chemical conditions unfaformation of magnesian vourable to the minerals. The MCF appears thus as a peculiar depositional environment combining restricted conditions in a coastal embayment, in relation to the palaeogeographical context and optimum climate conditions (LLTM), promoting enhanced microbial activity, highly variable circumneutral to high pH, high Mg and Si activities, favourable to early fibrous clay and dolomite formation.

CONCLUSION

In the Paris Basin, the late Lutetian is marked by a change from a marine-influenced bay to a shallow schizohaline coastal bay, where the restricted coastal bay is characterized by microbial activity. pedogenesis and evaporite precipitation. The coastal bay records a mineralogical transition from the calcite-dominated marine-influenced bay, with low clay content dominated by smectite and illite, to more restricted environments where microcrystalline dolomite and Mg-fibrous clays (palygorskite and sepiolite) predominate. The neoformation of Mg-clays by the transformation of a detrital Al-Fe-smectite precursor, controlled by a high Si/Mg ratio, is the predominant mechanism for palygorskite formation, which is counterbalanced by concomitant early dolomite formation. In the restricted coastal bay, dolomite formation may result from two processes: (i) direct precipitation of dolomite under microbial influence; (ii) dolomite formation through the ageing of a very high-magnesium calcite precursor, directly precipitated under microbial influence. In reaction to slightly more acidic conditions or during early diagenesis, dolomite dissolution may be an additional process, leading to palygorskite formation in relation to local chemical changes. These processes, promoted by microbial activity, require high ionic concentration, rapidly changing pH with predominantly alkaline conditions and high availability of fine detrital material. Such physico-biochemical conditions were brought together during the late Lutetian-early Bartonian in the Paris Basin by the following combination of palaeogeographical and climatic factors: (i) Pyrenean deformation resulting in a restricted shallow flat and preferably carbonated environment and (ii) a predominantly arid climate, punctuated by occasional run-off episodes further inland, resulting in schizohaline conditions. The major mineralogical change recorded in the 'Marnes et Caillasses' Formation, highlighted by Mg-fibrous clays and carbonate mineralogy during the late Lutetian-early Bartonian, reveals unique conditions exacerbated by the Late Lutetian Thermal Maximum (LLTM), recognized here for the first time in the coastal settings of the Paris Basin. The climate conditions induced by the LLTM cannot, however, be considered as the only trigger for the formation of dolomite and palygorskite, but would rather have facilitated these processes, in association with the palaeogeography of the Paris Basin, marked by a persistent shallow water system. Based on observations of these restricted coastal environments, this study proposes a comprehensive model to explain the concomitant formation of palygorskite and dolomite, influenced by microbial activity and highly fluctuating hydro-biogeochemical conditions.

ACKNOWLEDGEMENTS

This work is part of Julien Talon's PhD thesis, financially supported by the Région Bourgogne Franche-Comté (France), the University of Mons (Belgium) and the 'RGF Bassin parisien' programme of the Bureau de Recherches Géologiques et Minières (BRGM). It was also sponsored by an IAS postgraduate grant. We thank the three anonymous reviewers and the two Associate Editors for their helpful and constructive comments. We are grateful to Anne-Lise Santoni, Justine Blondet, Théo Martinez and all the staff of the GISMO, ARCEN and DImaCell platforms for their help during data acquisition. The BPE Lecieux company is thanked for providing access to the Saint-Maximin outcrop. Thanks to Marie-Pierre Aubry

and Chantal Bourdillon for discussions about the biostratigraphic framework of this study. John W. Valley (University of Wisconsin-Madison, USA) is thanked for providing the calcite and dolomite SIMS standards. Carmela Chateau-Smith is thanked for her help in improving the quality of the English in this manuscript. The research of AI was supported by the State program of the Geological Institute of Russian Academy of Sciences.

DATA AVAILABILITY STATEMENT

The data supporting the findings of this study are available in the Supporting Information of this article.

REFERENCES

- **Abrard, R.** (1925) Le lutétien du bassin de Paris: essai de monographie statigraphique, p. 388. Société française d'imprimerie d'Angers, Angers, France.
- Arenas, C. and Pomar, L. (2010) Microbial deposits in upper Miocene carbonates, Mallorca, Spain. Palaeogeogr. Palaeoclimatol. Palaeoecol.. 297, 465–485.
- Arnould, M., Deveughele, M. and Gigan, J.-P. (1971) Relations entre compositiion, texture et certaines propriétés géotechniques des "Marnes et Caillasses" du Lutétien supérieur du plateau de la Défense (Haut de Seine). *CR Acad. Sci. Paris, D*, **273**, 2195–2198.
- Asch, K. (2005) IGME 5000: 1:5 Million International Geological Map of Europe and Adjacent Areas. BGR (Hannover). Available at: https://www.bgr.bund.de/EN/Themen/Sammlungen-Grundlagen/GG_geol_Info/Karten/Europa/IGME5000/igme5000_node_en.html.
- Aubry, M.-P. (1986) Paleogene calcareous nannoplankton biostratigraphy of northwestern Europe. *Palaeogeogr. Palaeoclimatol. Palaeoecol.*, 55, 267–334.
- Auffret, J.P., Bignot, G. and Blondeau, A. (1975) Géologie du bassin tertiaire de la Manche orientale au large du Pays de Caux. Phil. Trans. R. Soc. Lond. A Math. Phys. Eng. Sci., 279, 169–176.
- Baumann, H. and Smith, E.M. (2018) Quantifying metabolically driven PH and oxygen fluctuations in US nearshore habitats at diel to interannual time scales. *Estuaries Coast*, 41, 1102–1117.
- Bignot, G., Hommeril, P. and Larsonneur, C. (1968) Le Lutétien au large du Cotentin. Bur. Rech. Géol. Min. Mém., 25, 405–417.
- **Birsoy, R.** (2002) Formation of sepiolite-palygorskite and related minerals from solution. *Clays Clay Miner.*, **50**, 736–745.
- Blondeau, A. (1965) Le Lutétien des Bassins de Paris, de Belgique et du Hampshire. Etude sédimentologique et paléontologique. PhD Thesis. Université de Paris, Paris.
- Bontognali, T.R.R., Vasconcelos, C., Warthmann, R.J., Bernasconi, S.M., Dupraz, C., Strohmenger, C.J. and McKenzie, J.A. (2010) Dolomite formation within microbial mats in the coastal sabkha of Abu Dhabi (United Arab Emirates): dolomite formation within microbial mats. Sedimentology, 57, 824–844.

- Bontognali, T.R.R., Vasconcelos, C., Warthmann, R.J., Lundberg, R. and McKenzie, J.A. (2012) Dolomitemediating bacterium isolated from the sabkha of Abu Dhabi (UAE). Terra Nova. 24, 248–254.
- Bontognali, T.R.R., McKenzie, J.A., Warthmann, R.J. and Vasconcelos, C. (2014) Microbially influenced formation of Mg-calcite and Ca-dolomite in the presence of exopolymeric substances produced by sulphate-reducing bacteria. *Terra Nova*, 26, 72–77.
- Bouton, A., Vennin, E., Pace, A., Bourillot, R., Dupraz, C., Thomazo, C., Brayard, A., Désaubliaux, G. and Visscher, P.T. (2016) External controls on the distribution, fabrics and mineralization of modern microbial mats in a coastal hypersaline lagoon, Cayo Coco (Cuba). Sedimentology, 63, 972-1016.
- Boyd, R., Dalrymple, R.W. and Zaitlin, B.A. (2006) Estuarine and incised-valley facies models. In: Facies Models Revisited (Eds Posamentier, H.W. and Walker, R.G.), SEPM Society for Sedimentary Geology, 84, 171.
- Brachert, T.C., Agnini, C., Gagnaison, C., Gély, J.-P., Henehan, M.J. and Westerhold, T. (2023) Astronomical pacing of middle eocene sea-level fluctuations: inferences from shallow-water carbonate ramp deposits. *Paleoceanogr. Paleoclimatol.*, 38, e2023PA004633.
- **Bradley, W.F., Burst, J.F.** and **Graf, D.L.** (1953) Crystal chemistry and differential thermal effect of dolomite. *Am. Mineral.*, **38**, 207–217.
- Briais, J. (2015) Le Cénozoïque du Bassin de Paris: un enregistrement sédimentaire haute résolution des déformations lithosphériques en régime de faible subsidence. PhD Thesis. Université de Rennes 1, Rennes.
- Briais, J., Guillocheau, F., Lasseur, E., Robin, C., Châteauneuf, J.J. and Serrano, O. (2016) Response of a low-subsiding intracratonic basin to long wavelength deformations: the Palaeocene–early Eocene period in the Paris Basin. Solid Earth, 7, 205–228.
- Briard, J., Pucéat, E., Vennin, E., Daëron, M., Chavagnac, V., Jaillet, R., Merle, D. and de Rafélis, M. (2020) Seawater paleotemperature and paleosalinity evolution in neritic environments of the Mediterranean margin: Insights from isotope analysis of bivalve shells. *Palaeogeogr., Palaeoclimatol., Palaeoecol.*, **543**, 109582.
- Brinkhuis, H. (1994) Late Eocene to Early Oligocene dinoflagellate cysts from the Priabonian type-area (Northeast Italy): biostratigraphy and paleoenvironmental interpretation. *Palaeogeogr. Palaeoclimatol. Palaeoecol.*, 107, 121–163.
- Broekman, J.A. (1984) Sedimentation and paleoecology of the Middle Eocene carbonates of the Paris Region. Proc. K. Ned. Akad. Wet. Ser. B, 87, 271–299.
- Brown, G. and Brindley, G.W. (1980) X-ray diffraction procedures for clay mineral identification. In: *Crystal Structures of Clay Minerals and their X-Ray Identification* (Eds Brindley, G.W. and Brown, G.), *Mineralogical Society of Great Britain and Ireland*, 5, 148.
- Brunet, M. and Le Pichon, X. (1982) Subsidence of the Paris Basin. J. Geophys. Res., 87, 8547–8560.
- Caillière, S., Arnould, M., Mathieu, A. and Moglia, G. (1966) Sur la nature essentiellement dolomitique et palygorskitique des Marnes et Caillasses du plateau de la Défense (Haut de Seine). CR Acad. Sci. Paris, D, 262, 1821–1823.
- Carmeille, M., Bourillot, R., Brunet, M.-F., Pellenard, P., Fürsich, F.T., Schnyder, J., Barrier, E., Blanpied, C. and Sidorova, I. (2018) Architecture and sedimentary

- evolution of the southwestern Gissar carbonate platform (Uzbekistan) during the Middle–Late Jurassic. *Mar. Petrol. Geol.*, **97**, 437–465.
- Cattaneo, A. and Steel, R.J. (2003) Transgressive deposits: a review of their variability. Earth Sci. Rev., 62, 187–228.
- Cavalcante, F., Belviso, C., Bentivenga, M., Fiore, S. and Prosser, G. (2011) Occurrence of palygorskite and sepiolite in upper Paleocene—middle Eocene marine deep sediments of the Lagonegro Basin (Southern Apennines—Italy): paleoenvironmental and provenance inferences. Sed. Geol., 233, 42–52.
- Cavelier, C. (1963) Sur les argiles fibreuses du bassin de Paris, C. R. Somm. Soc. Géol. Fr., 20, 125–127.
- Cavelier, C. (1968) Coupes détaillées des sondages exécutés dans le Paléogène du Bassin de Paris à Chaignes (Eure), Montjavoult (Oise), Cires-lès-Mello Le Tillet (Oise), Ludes (Marne). Bur. Rech. Géol. Min. Mém., 2, 13–52.
- Cavelier, C. and Le Calvez, Y. (1965) Presence d'Arenagula kerfornei (Allix), foraminifere "biarritzien", a la partie terminale du Lutetien superieur de Foulangues (Oise). Bull. Soc. Géol. Fr., 7, 284–286.
- Cavelier, C. and Pomerol, C. (1979) Chronologie et interpretation des evenements tectoniques cenozoiques dans le Bassin de Paris. Bull. Soc. Géol. Fr., S7-XXI, 33–48.
- Chamley, H. (1989) Clay Sedimentology, p. 623. Springer-Verl, Berlin, Heidelberg, Paris.
- Chen, T., Xu, H., Lu, A., Xu, X., Peng, S. and Yue, S. (2004)
 Direct evidence of transformation from smectite to
 palygorskite: TEM investigation. Sci. China Ser. D-Earth
 Sci., 47, 985–994.
- Clark, A.J., Vellekoop, J. and Speijer, R.P. (2022) Hydrological differences between the Lutetian Paris and Hampshire basins revealed by stable isotopes of conid gastropods. *Bull. Soc. Géol. Fr.*, **193**, 3.
- Court, W.M., Paul, A. and Lokier, S.W. (2017) The preservation potential of environmentally diagnostic sedimentary structures from a coastal sabkha. Mar. Geol., 386, 1–18.
- Cui, H., Kitajima, K., Orland, I.J., Baele, J.-M., Xiao, S., Kaufman, A.J., Denny, A., Spicuzza, M.J., Fournelle, J.H. and Valley, J.W. (2022) An authigenic response to Ediacaran surface oxidation: Remarkable micron-scale isotopic heterogeneity revealed by SIMS. *Precambrian Res.*, 377, 106676.
- Cupertino, D.F., Ramnani, C.W., Vanden Berg, M.D. and Awramik, S.M. (2024) Formation of magnesium-clay in a lacustrine microbialite-bearing carbonate deposit, Eocene Green River Formation, Sanpete County, Utah. Sedimentology, 71, 263–292.
- **Deconinck, J.F., Strasser, A.** and **Debrabant, P.** (1988) Formation of illitic minerals at surface temperatures in Purbeckian sediments (Lower Berriasian, Swiss and French Jura). *Clay Miner.*, **23**, 91–103.
- Deelman, J.C. (1999) Low-temperature nucleation of magnesite and dolomite. Neues Jahrb. Mineral. Monatsh., 2. 289–302.
- Del Buey, P., Cabestrero, Ó., Arroyo, X. and Sanz-Montero, M.E. (2018) Microbially induced palygorskite-sepiolite authigenesis in modern hypersaline lakes (Central Spain). Appl. Clay Sci., 160, 9–21.
- Del Buey, P., Sanz-Montero, M.E., Braissant, O., Cabestrero, Ó. and Visscher, P.T. (2021) The role of microbial extracellular polymeric substances on formation of sulfate minerals and fibrous Mg-clays. Chem. Geol., 581, 120403.

- Del Buey, P., Sanz-Montero, M.E. and Sánchez-Román, M. (2023) Bioinduced precipitation of smectites and carbonates in photosynthetic diatom-rich microbial mats: Effect of culture medium. Appl. Clay Sci., 238, 106932.
- Del Buey, P., Sanz-Montero, M.E., Rodríguez-Aranda, J.P., Sánchez-Román, M. and Nieto, F. (2025) The Miocene Source-to-Sink Evolution of Fibrous Clay Minerals in Hyperalkaline Playa-Lakes, Duero Basin (Central Spain). *Minerals*, **15**, 50.
- DiLoreto, Z.A., Bontognali, T.R.R., Al Disi, Z.A., Al-Kuwari, H.A.S., Williford, K.H., Strohmenger, C.J., Sadooni, F., Palermo, C., Rivers, J.M., McKenzie, J.A., Tuite, M. and Dittrich, M. (2019) Microbial community composition and dolomite formation in the hypersaline microbial mats of the Khor Al-Adaid sabkhas, Qatar. *Extremophiles*, 23, 201–218.
- Diloreto, Z.A., Garg, S., Bontognali, T.R.R. and Dittrich, M. (2021) Modern dolomite formation caused by seasonal cycling of oxygenic phototrophs and anoxygenic phototrophs in a hypersaline sabkha. *Sci. Rep.*, 11, 4170.
- Draidia, S., El Ouahabi, M., Daoudi, L., Havenith, H.-B. and Fagel, N. (2016) Occurrences and genesis of palygorskite/sepiolite and associated minerals in the Barzaman formation, United Arab Emirates. *Clay Miner.*, 51, 763–779.
- Eberl, D.D., Środoń, J. and Northrop, H.R. (1987) Potassium fixation in smectite by wetting and drying. *Geochem. Process. Min. Surf.*, **323**, 296–326.
- Edgar, K.M., Wilson, P.A., Sexton, P.F. and Suganuma, Y. (2007) No extreme bipolar glaciation during the main Eocene calcite compensation shift. *Nature*, **448**, 908–911.
- Egal, E. (2023) New elements on the lithostratigraphy of the Paris Eocene series based on the observation of hundreds of core drillings (Eole and Grand Paris Express projects). *Géologie de la France*, **4**, 63–86.
- El Ali, A., Barbin, V., Calas, G., Cervelle, B., Ramseyer, K. and Bouroulec, J. (1993) Mn²⁺-activated luminescence in dolomite, calcite and magnesite: quantitative determination of manganese and site distribution by EPR and CL spectroscopy. *Chem. Geol.*, **104**, 189–202.
- Erdtman, G. (1960) The acetolysis method, a revised description. Svensk Bot. Tidskr., 56, 561-564.
- Esteoule-Choux, J. (1970) Contribution à l'étude des argiles du Massif armoricain: argiles des altérations et argiles des bassins sédimentaires tertiaires, p. 319. Institut de géologie, Rennes.
- Esteoule-Choux, J. (1984) Palygorskite in the tertiary deposits of the Armorican Massif. *Dev. Sedimentol.*, **37**, 75–85.
- Fagel, N. (2007) Chapter four clay minerals, deep circulation and climate. In: *Developments in Marine Geology*, pp. 139–184. Elsevier, New York, NY.
- Fang, Y. and Xu, H. (2022) Dissolved silica-catalyzed disordered dolomite precipitation. Am. Mineral., 107, 443–452.
- Fesharaki, O., García-Romero, E., Cuevas-González, J. and López-Martínez, N. (2007) Clay mineral genesis and chemical evolution in the Miocene sediments of Somosaguas, Madrid Basin, Spain. Clay Miner., 42, 187–201.
- Flügel, E. (2004) Microfacies of Carbonate Rocks: Analysis, Interpretation and Application, p. 976. Springer Science & Business Media, Berlin, Heidelberg.
- Folk, R.L. and Land, L.S. (1975) Mg/Ca ratio and salinity: two controls over crystallization of dolomite. AAPG Bull., 2, 564–568.
- Folk, R.L. and Siedlecka, A. (1974) The "schizohaline" environment: Its sedimentary and diagenetic fabrics as

- exemplified by Late Paleozoic rocks of Bear Island, Svalbard. Sed. Geol., 11, 1–15.
- Fontes, J.C. and Toulemont, M. (1987) Faciès, pétrologie et teneurs en isotopes lourds (18O, 13C, 34S) des niveaux évaporitiques du Lutétien supérieur du Bassin de Paris: interprétation paléohydrologique. Bull. Centres Rech. Explor.-Prod. Elf-Aquitaine, 11, 39–64.
- Fontes, J.C., Fritz, P. and Letolle, R. (1970) Composition isotopique, mineralogique et genèse des dolomies du Bassin de Paris. *Geochim. Cosmochim. Acta*, **34**, 279–294.
- Fulignati, P. (2020) Clay minerals in hydrothermal systems. Minerals, 10, 919.
- Galán, E. and Pozo, M. (2011) Palygorskite and sepiolite deposits in continental environments. Description, genetic patterns and sedimentary settings. In: *Developments in Clay Science*, pp. 125–173. Elsevier, London.
- Galán, E. and Singer, A. (2011) Developments in palygorskite-sepiolite research: a new outlook on these nanomaterials, 1st edn, p. 270. Elsevier, Oxford.
- García-Romero, E. and Suárez, M. (2013) Sepiolite-palygorskite: Textural study and genetic considerations. Appl. Clay Sci., 86, 129–144.
- Gély, J.-P. (1996) Le Lutétien du Bassin parisien: de l'analyse séquentielle haute-résolution à la reconstitution paléogéographique. Bull. Inf. Géol. Bassin Paris, 34, 3–27.
- Gély, J.-P. (2016) Le Paléogène du Bassin de Paris: Corrélations et reconstitutions paléogéographiques. Bull. Inf. Géol. Bassin Paris. 53, 2–13.
- Gerdes, G. and Krumbein, W.E. (Eds) (1987) Biolaminated Deposits. Springer-Verlag, Berlin/Heidelberg.
- Gillhaus, A., Richter, D.K., Götte, T. and Neuser, R.D. (2010)
 From tabular to rhombohedral dolomite crystals in
 Zechstein 2 dolostones from Scharzfeld (SW
 Harz/Germany): a case study with combined CL and EBSD
 investigations. Sed. Geol., 228, 284–291.
- Goldsmith, J.R. and Graf, D.L. (1958) Structural and compositional variations in some natural dolomites. J. Geol., 66, 678–693.
- Gregg, J.M., Bish, D.L., Kaczmarek, S.E. and Machel, H.G. (2015) Mineralogy, nucleation and growth of dolomite in the laboratory and sedimentary environment: a review. Sedimentology, 62, 1749–1769.
- Guggenheim, S. and Krekeler, M.P.S. (2011) The Structures and Microtextures of the Palygorskite–Sepiolite Group Minerals. In: *Developments in Clay Science*, pp. 3–32. Elsevier, London.
- Guillocheau, F., Robin, C., Allemand, P., Bourquin, S.,
 Brault, N., Dromart, G., Friedenberg, R., Garcia, J.-P.,
 Gaulier, J.-M., Gaumet, F., Grosdoy, B., Hanot, F., Le
 Strat, P., Mettraux, M., Nalpas, T., Prijac, C., Rigolet, C.,
 Serrano, O. and Grandjean, G. (2000) Meso-Cenozoic
 geodynamic evolution of the Paris Basin: 3D stratigraphic
 constraints. Geodin. Acta, 13, 189-245.
- Guo, P., Wen, H. and Sánchez-Román, M. (2023a) Constraints on dolomite formation in a Late Palaezoic saline alkaline lake deposit, Junggar Basin, north-west China. Sedimentology, 70, 2302–2330.
- Guo, P., Wen, H., Li, C., He, H. and Sánchez-Román, M. (2023b) Lacustrine dolomite in deep time: What really matters in early dolomite formation and accumulation? *Earth Sci. Rev.*, 246, 104575.
- Hao, O.J., Chen, J.M., Huang, L. and Buglass, R.L. (1996) Sulfate-reducing bacteria. Crit. Rev. Environ. Sci. Technol., 26, 155–187.

- Haq, B.U., Hardenbol, J., Vail, P.R., Stover, L.E., Colin, J.P., Ioannides, N.S., Wright, R.C., Baum, G.R., Gombos, A.M., Jr., Pflum, C.E., Loutit, T.S., du Chêne, R.J., Romine, K.K., Sarg, J.F., Posamentier, H.W. and Morgan, B.E. (1988) Mesozoic and Cenozoic Chronostratigraphy and Cycles of Sea-Level Change. In: Sea-Level Changes: An Integrated Approach (Eds Wilgus, C.K., Hastings, B.S., Posamentier, H., Wagoner, J.V., Ross, C.A. and Kendall, C.G.S.C.), SEPM Society for Sedimentary Geology, 42, 71.
- Hillier, S. (2000) Accurate quantitative analysis of clay and other minerals in sandstones by XRD: comparison of a Rietveld and a reference intensity ratio (RIR) method and the importance of sample preparation. *Clay Miner.*, **35**, 291–302.
- Hips, K., Haas, J., Poros, Z., Kele, S. and Budai, T. (2015) Dolomitization of Triassic microbial mat deposits (Hungary): Origin of microcrystalline dolomite. Sed. Geol., 318, 113–129.
- Hobbs, F.W.C., Fang, Y., Lebrun, N., Yang, Y. and Xu, H. (2024) Co-precipitation of primary dolomite and Mg-rich clays in Deep Springs Lake, California. Sedimentology, 6, 1363-1383.
- Hong, H.L., Yu, N., Xiao, P., Zhu, Y.H., Zhang, K.X. and Xiang, S.Y. (2007) Authigenic palygorskite in Miocene sediments in Linxia basin, Gansu, northwestern China. Clay Miner., 42, 45–58.
- Huggett, J.M. and Knox, R.W.O. (2006) Clay mineralogy of the Tertiary onshore and offshore strata of the British Isles. Clay Miner., 41, 5–46.
- Iacoviello, F., Giorgetti, G., Nieto, F. and Memmi, I.T. (2012) Evolution with depth from detrital to authigenic smectites in sediments from AND-2A drill core (McMurdo Sound, Antarctica). Clay Miner., 47, 481–498.
- Iakovleva, A.I., Quesnel, F. and Dupuis, C. (2021) New insights on the Late Paleocene Early Eocene dinoflagellate cyst zonation for the Paris and Dieppe basins. Bull. Soc. Géol. Fr., 192, 21035.
- Illing, L. and Taylor, J. (1993) Penecontemporaneous Dolomitization in Sabkha Faishakh, Qatar: Evidence from Changes in the Chemistry of the Interstitial Brines. *J. Sediment. Res.*, **2**, 865.
- Inglès, M. and Anadón, P. (1991) Relationship of clay minerals to depositional environment in the non-marine Eocene Pontils Group, Se Ebro Basin (Spain). J. Sediment. Res., 78, 1865.
- Intxauspe-Zubiaurre, B., Martínez-Braceras, N., Payros, A., Ortiz, S., Dinarès-Turell, J. and Flores, J.-A. (2018) The last Eocene hyperthermal (Chron C19r event, ~41.5 Ma): chronological and paleoenvironmental insights from a continental margin (Cape Oyambre, N Spain). *Palaeogeogr. Palaeoclimatol. Palaeoecol.*, **505**, 198–216.
- **Isphording, W.C.** (1973) Discussion of the occurrence and origin of sedimentary palygorskite-sepiolite deposits. *Clay Clay Mineral.*, **21**, 391–401.
- **Jones, B.F.** and **Conko, K.M.** (2011) Environmental influences on the occurrences of sepiolite and palygorskite: a brief review. *Develop. Clay Sci.*, **3**, 69–83.
- Kaczmarek, S.E., Gregg, J.M., Bish, D.L., Machel, H.G. and Fouke, B.W. (2017) Dolomite, Very High-Magnesium Calcite, and microbes implications for the microbial model of dolomitization. In: *Characterization and Modeling of Carbonates–Mountjoy Symposium 1*. SEPM (Society for Sedimentary Geology), Tulsa, OK. https://doi.org/10.2110/sepmsp.109.01.

- Kadir, S., Erkoyun, H., Eren, M., Huggett, J. and Önalgil, N. (2016) Mineralogy, geochemistry, and genesis of sepiolite and palygorskite in Neogene Lacustrine Sediments, Eskişehir Province, West Central Anatolia, Turkey. Clays Clay Miner., 64, 145–166.
- **Kennard, J.M.** and **James, N.P.** (1986) Thrombolites and stromatolites: two distinct types of microbial structures. *Palaios*, **1**, 492.
- King, C. (2006) Paleogene and Neogene: uplift and a cooling climate. In: The Geology of England and Wales (Eds Brenchley, P.J. and Rawson, P.F.), pp. 395–427. The Geological Society of London, London.
- Kirkham, A. and Huggett, J.M. (2020) Quaternary palygorskite-dolomite occurrences in Abu Dhabi Emirate. Arab. J. Geosci., 13, 290.
- Knox, R.W.O., Bosch, J.H.A., Rasmussen, E.S., Heilmann-Clausen, C., Hiss, M., De Lugt, I.R., Kasińksi, J., King, C., Köthe, A., Słodkowska, B., Standke, G. and Vandenberghe, N. (2010) Cenozoic. In: Petroleum Geological Atlas of the Southern Permian Basin Area (Eds Doornenbal, J.C. and Stevenson, A.G.), pp. 211–223. EAGE Publications, Houten.
- Koschorreck, M. (2008) Microbial sulphate reduction at a low pH: microbial sulphate reduction at low pH. FEMS Microbiol. Ecol., 64, 329–342.
- Krause, S., Liebetrau, V., Gorb, S., Sánchez-Román, M., McKenzie, J.A. and Treude, T. (2012) Microbial nucleation of Mg-rich dolomite in exopolymeric substances under anoxic modern seawater salinity: New insight into an old enigma. Geology, 40, 587–590.
- Krumgalz, B. (1980) Chapter 6 salt effect on the pH of hypersaline solutions. Develop. Sedimentol., 28, 73–83.
- Le Calvez, Y. (1968) Les foraminifères du Paléogène des sondages de Chaignes, Montjavoult, Cires-lès-Mello - Le Tillet et Ludes (Bassin de Paris). Bur. Rech. Géol. Min. Mém., 45, 101–106.
- Li, X., Li, F., Wang, J., Wang, B., Wang, Z., Sun, X., Qian, L. and Yi, C. (2022) Formation and preservation of Eocene lacustrine microbialites in the western Qaidam Basin (northeastern Qinghai-Tibetan Plateau, China): Petrological, mineralogical, and geochemical constraints. Sed. Geol., 440, 106257.
- Liu, D., Xu, Y., Papineau, D., Yu, N., Fan, Q., Qiu, X. and Wang, H. (2019) Experimental evidence for abiotic formation of low-temperature proto-dolomite facilitated by clay minerals. Geochim. Cosmochim. Acta, 247, 83–95.
- Lokier, S.W. (2013) Coastal Sabkha Preservation in the Arabian Gulf. *Geoheritage*, 5, 11–22.
- Lopez-Galindo, A., Ben Aboud, A., Fenoll Hach-Ali, P. and Casas Ruiz, J. (1996) Mineralogical and geochemical characterization of palygorskite from Gabasa (NE Spain). Evidence of a detrital precursor. Clay Miner., 31, 33–44.
- Lumsden, D.N. (1979) Discrepancy between thin-section and X-ray estimates of dolomite in limestone. J. Sediment. Res., 25, 1865.
- Machel, H.G. (2001) Bacterial and thermochemical sulfate reduction in diagenetic settings — old and new insights. Sed. Geol., 140, 143–175.
- Machel, H.G. (2004) Concepts and models of dolomitization: a critical reappraisal. *Geol. Soc. Lond. Spec. Publ.*, **235**, 7–63.
- Manaa, A.A. and Aref, M.A. (2022) Microbial mats and evaporite facies variation in a supralittoral, ephemeral lake, Red Sea coast, Saudi Arabia. *Facies*, **68**, 641.
- Marie, N. (2023) Faciès sédimentaires et géométries 3D à haute résolution dans un bassin faiblement subsident: le

- cas du Bartonien du Bassin de Paris. PhD Thesis. Université de Rennes, Rennes.
- Mather, C.C., Lampinen, H.M., Tucker, M., Leopold, M., Dogramaci, S., Raven, M. and Gilkes, R.J. (2023) Microbial influence on dolomite and authigenic clay mineralisation in dolocrete profiles of NW Australia. *Geobiology*, 21, 644–670.
- McCormack, J., Baldermann, A., Bontognali, T.R.R., Wolf, A. and Kwiecien, O. (2024) Hydrochemical mixing-zones trigger dolomite formation in an alkaline lake. Sedimentology, 71, 871–886.
- McKenzie, J.A. (1981) Holocene dolomitization of calcium carbonate sediments from the Coastal Sabkhas of Abu Dhabi, U.A.E.: a stable isotope study. *J. Geol.*, **89**, 185–198.
- McKenzie, J.A. and Vasconcelos, C. (2009) Dolomite Mountains and the origin of the dolomite rock of which they mainly consist: historical developments and new perspectives. *Sedimentology*, **56**, 205–219.
- Mégnien, C. and Mégnien, F. (Eds) (1980) Synthèse géologique du bassin de Paris. Éditions du B.R.G.M, Orléans.
- Mercier-Castiaux, M., Chamley, H. and Dupuis, C. (1988) La sédimentation argileuse tertiaire dans le bassin belge et ses approches occidentales. *Ann. Soc. Géol. Nord*, CVII, 139–154.
- Meulenkamp, J.E., Sissingh, W., Calvo, J.P., Daams, S., Londeix, L., Cahuzac, B., Kovac, M., Nagymarosy, A., Rusu, A., Badescu, D., Beniamovskii, V.N., Scherba, I.G., Roger, J., Platel, J.P., Hirsch, F., Sadek, A., Abdel-Gawad, G.I., Ben Ismail-Lattrache, K., Zaghbib-Turki, D., Bouaziz, S., Karoui-Yaakoub, N. and Yaich, C. (2000) Late Lutetian (44-41 Ma). In: Atlas Peri-Tethys, Palaeogeographical Maps (Eds Dercourt, J., Gaetani, M., Vrielynck, B., Barrier, E., Biju-Duval, B., Brunet, M.-F., Cadet, J.-P., Crasquin, S. and Sandulescu, M.), pp. 163–170. CCGM/CGMW, Paris.
- Molnár, Z., Pekker, P., Dódony, I. and Pósfai, M. (2021) Clay minerals affect calcium (magnesium) carbonate precipitation and aging. Earth Planet. Sci. Lett., 567, 116971
- Moore, D.M. and Reynolds, R.C. (1997) X-Ray Diffraction and the Identification and Analysis of Clay Minerals, 2nd edn, p. 378. Oxford University Press, Oxford; New York.
- Moore, T.S., Murray, R.W., Kurtz, A.C. and Schrag, D.P. (2004) Anaerobic methane oxidation and the formation of dolomite. Earth Planet. Sci. Lett., 229, 141–154.
- Moreau, K. (2023) Caractérisation des hétérogénéités réservoirs dans les carbonates continentaux du Cénozoïque du Bassin de Paris: Liens entre faciès sédimentaire, diagenèse et propriétés pétrophysiques. PhD Thesis. Université Paris Saclay, Paris.
- Moreau, K., Andrieu, S., Briais, J., Brigaud, B. and Ader, M. (2024) Facies distribution and depositional cycles in lacustrine and palustrine carbonates: The Lutetian–Aquitanian record in the Paris Basin. *Depos. Rec.*, **10**, 124–158.
- Neuhuber, S., Gier, S., Draganits, E., Steier, P., Bolka, M., Ottner, F., Spötl, C., Hippler, D. and Meister, P. (2024) Radiocarbon ages of microcrystalline authigenic carbonate in Lake Neusiedl (Austria) suggest millennial-scale growth of Mg-calcite and protodolomite. *Sedimentology*, **71**, 912–940.
- Pace, A., Bourillot, R., Bouton, A., Vennin, E., Galaup, S., Bundeleva, I., Patrier, P., Dupraz, C., Thomazo, C., Sansjofre, P., Yokoyama, Y., Franceschi, M., Anguy, Y., Pigot, L., Virgone, A. and Visscher, P.T. (2016) Microbial

- and diagenetic steps leading to the mineralisation of Great Salt Lake microbialites. *Sci. Rep.*, **6**, 31495.
- Perri, E., Tucker, M.E., Słowakiewicz, M., Whitaker, F., Bowen, L. and Perrotta, I.D. (2018) Carbonate and silicate biomineralization in a hypersaline microbial mat (Mesaieed sabkha, Qatar): Roles of bacteria, extracellular polymeric substances and viruses. Sedimentology, 65, 1213–1245.
- Petrash, D.A., Bialik, O.M., Bontognali, T.R.R., Vasconcelos, C., Roberts, J.A., McKenzie, J.A. and Konhauser, K.O. (2017) Microbially catalyzed dolomite formation: from near-surface to burial. *Earth Sci. Rev.*, 171, 558–582.
- Petrash, D.A., Bialik, O.M., Staudigel, P.T., Konhauser, K.O. and Budd, D.A. (2021) Biogeochemical reappraisal of the freshwater–seawater mixing-zone diagenetic model. Sedimentology, 68, 1797–1830.
- Petschick, R. (2010) MacDiff 4.2.6 Manual. Available at: https://www.uni-frankfurt.de/69528130/Petschick__MacOS_ Software.
- Pineda, V., Gibert, L., Soria, J.M., Carrazana, A., Ibáñez-Insa, J. and Sánchez-Román, M. (2021) Interevaporitic deposits of Las Minas Gypsum Unit: a record of Late Tortonian marine incursions and dolomite precipitation in Las Minas Basin (eastern Betic Cordillera, SE Spain). Palaeogeogr. Palaeoclimatol. Palaeoecol., 564, 110171.
- Plint, A.G. (1983) Facies, environments and sedimentary cycles in the Middle Eocene, Bracklesham Formation of the Hampshire Basin: evidence for global sea-level changes? Sedimentology, 30, 625–653.
- Pomerol, C. (1967) Les minéraux argileux dans le tertiaire du bassin de Paris. Problèmes d'origine et de genèse. Bull. Groupe Français des Argiles, 19, 115–123.
- Pomerol, C. (1978) Evolution paléogéographique et structurale du Bassin de Paris, du Précambrien à l'actuel, en relation avec les régions avoisinantes. Geol. Mijnbouw, 57, 533-543.
- Pomerol, C. (1989) Stratigraphy of the Palaeogene: hiatuses and transitions. Proc. Geol. Assoc., 100, 313–324.
- Popa, R., Kinkle, B.K. and Badescu, A. (2004) Pyrite framboids as biomarkers for iron-sulfur systems. *Geomicrobiol J.*, 21, 193–206.
- Powell, A.J. (1992) A Stratigraphic Index of Dinoflagellate Cysts. British Micropaleontological Society Publication Series, Keyworth.
- Pozo, M. and Calvo, J. (2018) An Overview of Authigenic Magnesian Clays. Minerals, 8, 520.
- Quesnel, F., Storme, J.-Y., Roche, E., Iakovleva, A., Missiaen, P., Smith, T., Bourdillon, C., Baele, J.-M., Yans, J., Schnyder, J., Iacumin, P., Fléhoc, C. and Dupuis, C. (2014) An unexpected record of the PETM in terrestrial and organic sediments of Avesnois, between the Paris and Belgian Basins, NW Europe. Rend. Soc. Geol. Ital., 31, 183–184.
- Raven, J.A. (1991) Physiology of inorganic C acquisition and implications for resource use efficiency by marine phytoplankton: relation to increased CO₂ and temperature. Plant Cell Environ., 14, 779–794.
- Raven, J.A., Gobler, C.J. and Hansen, P.J. (2020) Dynamic CO₂ and pH levels in coastal, estuarine, and inland waters: Theoretical and observed effects on harmful algal blooms. *Harmful Algae*, **91**, 101594.
- Reeder, R.J. and Prosky, J.L. (1986) Compositional Sector Zoning in Dolomite. J. Sediment. Res., 25, 1865.
- Renard, M. (1972) Interprétation des teneurs en strontium des carbonates du Lutétien supérieur, à Saint-Vaast-les-Mello (Oise). Bull. Inf. Géol. Bassin Paris, 34, 19–29.

- Reynaud, J.-Y., Vennin, E., Parize, O., Rubino, J.-L. and Bourdillon, C. (2012) Incised valleys and tidal seaways: the example of the Miocene Uzès-Castillon basin, SE France. Bull. Soc. Géol. Fr., 183, 471–486.
- Richter, D.K., Götte, T., Götze, J. and Neuser, R.D. (2003)
 Progress in application of cathodoluminescence (CL) in sedimentary petrology. *Mineral. Petrol.*, **79**, 127–166.
- Rivero-Cuesta, L., Westerhold, T., Agnini, C., Dallanave, E., Wilkens, R.H. and Alegret, L. (2019) Paleoenvironmental changes at ODP site 702 (South Atlantic): anatomy of the middle eocene climatic optimum. *Paleoceanogr. Paleoclimatol.*, **34**, 2047–2066.
- Roche, E., Dupuis, C., Stambouli-Essassi, S., Russo-Ermolli, E., Putter, T.D., Nicaise, D. and Fairon-Demaret, M. (2008)
 Phytostratigraphie et paléoenvironnements du Néogène de l'Entre-Sambre-et- Meuse et du Condroz (Belgique).
 Evolution paléoclimatique du subtropical humide au tempéré froid. Geo-Eco-Trop, 25, 101–130.
- Ryan, B.H., Kaczmarek, S.E. and Rivers, J.M. (2019)
 Dolomite dissolution: an alternative diagenetic pathway for the formation of palygorskite clay. *Sedimentology*, **66**, 1803–1824
- Sánchez-Román, M., Vasconcelos, C., Warthmann, R., Rivadeneyra, M.A. and McKenzie, J.A. (2009a) Microbial Dolomite Precipitation under Aerobic Conditions: Results from Brejo do Espinho Lagoon (Brazil) and Culture Experiments. In: Perspectives in Carbonate Geology: A Tribute to the Career of Robert Nathan Ginsburg (Eds Swart, P.K., Eberli, G.P., McKenzie, J.A., Jarvis, I. and Stevens, T.), Sedimentology, (IAS Spec Publ No. 40), 25, 167–178.
- Sánchez-Román, M., McKenzie, J.A., de Luca Rebello Wagener, A., Rivadeneyra, M.A. and Vasconcelos, C. (2009b) Presence of sulfate does not inhibit low-temperature dolomite precipitation. *Earth Planet. Sci. Lett.*, **285**, 131–139.
- Sánchez-Román, M., Romanek, C.S., Fernández-Remolar, D.C., Sánchez-Navas, A., McKenzie, J.A., Pibernat, R.A. and Vasconcelos, C. (2011) Aerobic biomineralization of Mg-rich carbonates: Implications for natural environments. Chem. Geol., 281, 143–150.
- Sánchez-Román, M., Gibert, L., Martín-Martín, J.D., van Zuilen, K., Pineda-González, V., Vroon, P. and Bruggmann, S. (2023) Sabkha and salina dolomite preserves the biogeochemical conditions of its depositional paleoenvironment. *Geochim. Cosmochim. Acta*, **356**, 66–82.
- Sánchez-Román, M., Chandra, V., Mulder, S., Areias, C., Reijmer, J. and Vahrenkamp, V. (2025) The hidden role of heterotrophic bacteria in early carbonate diagenesis. *Sci. Rep.*, 15, 561.
- Serra-Kiel, J., Hottinger, L., Caus, E., Drobne, K., Ferrandez, C., Jauhri, A.K., Less, G., Pavlovec, R., Pignatti, J., Samso, J.M., Schaub, H., Sirel, E., Strougo, A., Tambareau, Y., Tosquella, J. and Zakrevskaya, E. (1998) Larger foraminiferal biostratigraphy of the Tethyan Paleocene and Eocene. *Bull. Soc. Géol. Fr.*, **169**, 281–299.
- Singer, A. (1979) Palygorskite in sediments: detrital, diagenetic or neoformed — A critical review. Geol. Rundsch., 68, 996–1008.
- **Singer**, **A.** (1984) Pedogenic palygorskite in the arid environment. *Dev. Sedimentol.*, **37**, 169–176.
- Singer, A. and Galan, E. (1984) Palygorskite-Sepiolite Occurrences, Genesis, and Uses, p. 352. Elsevier Distributors for the U.S. and Canada, Amsterdam New York New York, NY.

365391, 2025, 6, Downloaded from https://onlinelibrary.wiley.com/doi/10.1111/sed.70024 by Cochrane France, Wiley Online Library on [17/9/2025]. See the Terms and Conditions (https://onlinelibrary.wiley.com/terms-ad-conditions) on Wiley Online Library or uses (OA articles are governed by the applicable Cerative Commons Licenses

- Singer, A. and Norrish, K. (1974) Pedogenic palygorskite occurrences in Australia. Am. Mineral., 59, 508–517.
- Sissingh, W. (1998) Comparative tertiary stratigraphy of the Rhine Graben, Bresse Graben and Molasse Basin: correlation of Alpine foreland events. *Tectonophysics*, 300, 249–284.
- Sissingh, W. (2003) Tertiary paleogeographic and tectonostratigraphic evolution of the Rhenish Triple Junction. *Palaeogeogr. Palaeoclimatol. Palaeoecol.*, **196**, 229–263.
- Sluijs, A., Pross, J. and Brinkhuis, H. (2005) From greenhouse to icehouse; organic-walled dinoflagellate cysts as paleoenvironmental indicators in the Paleogene. *Earth Sci. Rev.*, 68, 281–314.
- Soyer, R. (1960) Les zones gypseuses anteludiennes preservees de l'Île-de-France. Bull. Soc. Géol. Fr., II, 145–151.
- Speijer, R.P., Pälike, H., Hollis, C.J., Hooker, J.J. and Ogg, J.G. (2020) The Paleogene Period. In: Geologic Time Scale 2020, pp. 1087–1140. Elsevier, London.
- Steurbaut, E., De Coninck, J. and Van Simaeys, S. (2016) Micropalaeontological dating of the Prémontré mammal fauna (MP10, Prémontré Sands, EECO, early late Ypresian, Paris Basin). Geol. Belg., 19, 273–280.
- Suarez, M., Martin Pozas, J.M., Robert, M. and Elsass, F. (1994) Evidence of a precursor in the neoformation of palygorskite new data by analytical electron microscopy. Clay Miner., 29, 255–264.
- Tazaki, K., Fyfe, W.S. and Heath, G.R. (1986) Palygorskite formed on montmorillonite in North Pacific deep-sea sediments. Clay Sci., 6, 197–216.
- Thiry, M. (1989) Geochemical evolution and paleoenvironments of the eocene continental deposits in the Paris Basin. Palaeogeogr., Palaeoclimatol., Palaeoecol., 70, 153–163.
- Toulemont, M. (1987) Les Gypses lutétiens du bassin de Paris: sédimentation, karstification et conséquences géotechniques, p. 318. Laboratoire Central des Ponts et Chaussées, Paris.
- **Trauth, N.** (1977) Argiles évaporitiques dans la sédimentation carbonatée continentale et épicontinentale tertiaire. Bassins de Paris, de Mormoiron et de Salinelles (France), Jbel Ghassoul (Maroc), 201 pp.
- Trauth, N., Lucas, J. and Sommer, F. (1968) Etude des minéraux argileux du Paléogène des sondages de Chaignes, Montjavoult, Le Tillet et Ludes (Bassin de Paris). Bur. Rech. Géol. Min. Mém., 56, 53–76.
- Valleron, M.M., Dulau, N., Pourzahed, P. and Saugrin, T. (1983) Calcitisations et opalitisations dans l'Eocene du Sud-Est de la France; Comparaison avec des facies analogues d'Alsace et de Touraine. Bull. Soc. Géol. Fr., S7-XXV, 11–18.
- Van Lith, Y., Warthmann, R., Vasconcelos, C. and Mckenzie, J.A. (2003) Sulphate-reducing bacteria induce low-temperature Ca-dolomite and high Mg-calcite formation. *Geobiology*, 1, 71–79.
- Van Wagoner, J.C., Mitchum, R.M., Campion, K.M. and Rahmanian, V.D. (1990) Siliciclastic Sequence Stratigraphy in Well Logs, Cores, and Outcrops: Concepts for High-Resolution Correlation of Time and Facies, Vol. 56, p. 77. American Association of Petroleum Geologists, Tulska, OK.
- Vasconcelos, C. and McKenzie, J.A. (1997) Microbial mediation of modern dolomite precipitation and diagenesis under anoxic conditions (Lagoa Vermelha, Rio de Janeiro, Brazil). J. Sediment. Res., 56, 1865.

- Vasconcelos, C., McKenzie, J.A., Bernasconi, S., Grujic, D. and Tiens, A.J. (1995) Microbial mediation as a possible mechanism for natural dolomite formation at low temperatures. *Nature*, 377, 220–222.
- Vennin, E., Bouton, A., Bourillot, R., Pace, A., Roche, A., Brayard, A., Thomazo, C., Virgone, A., Gaucher, E.C., Desaubliaux, G. and Visscher, P.T. (2019) The lacustrine microbial carbonate factory of the successive Lake Bonneville and Great Salt Lake, Utah, USA. Sedimentology, 66, 165–204.
- Wacey, D., Wright, D.T. and Boyce, A.J. (2007) A stable isotope study of microbial dolomite formation in the Coroong Region, South Australia. Chem. Geol., 244, 155– 174
- Wallace, R.B., Baumann, H., Grear, J.S., Aller, R.C. and Gobler, C.J. (2014) Coastal ocean acidification: the other eutrophication problem. *Estuar. Coast. Shelf Sci.*, **148**, 1–13.
- Warr, L.N. (2022) Earth's clay mineral inventory and its climate interaction: a quantitative assessment. Earth Sci. Rev., 234, 104198.
- Warthmann, R., van Lith, Y., Vasconcelos, C., McKenzie, J.A. and Karpoff, A.M. (2000) Bacterially induced dolomite precipitation in anoxic culture experiments. *Geology*, **28**, 1091–1094.
- Weaver, C.E. (1989) Clays, Muds, and Shales, p. 819. Elsevier, Distributors for the U.S. and Canada, Elsevier Science Pub. Co, Amsterdam; New York, NY.
- Weaver, C.E. and Beck, K.C. (1977) Miocene of the S.E. United States: a model for chemical sedimentation in a peri-marine environment. Sed. Geol., 17, IX-234.
- Weaver, C.E. and Pollard, L.D. (1973) The Chemistry of Clay Minerals, p. 213. Elsevier, Amsterdam.
- Wen, Y., Sanchez-Román, M., Li, Y., Wang, C., Han, Z., Zhang, L. and Gao, Y. (2020) Nucleation and stabilization of Eocene dolomite in evaporative lacustrine deposits from central Tibetan plateau. Sedimentology, 67, 3333–3354.
- Westerhold, T. and Röhl, U. (2013) Orbital pacing of Eocene climate during the Middle Eocene Climate Optimum and the chron C19r event: Missing link found in the tropical western Atlantic. *Geochem. Geophys. Geosyst.*, 14, 4811–4825.
- Westerhold, T., Röhl, U., Donner, B., Frederichs, T., Kordesch, W.E.C., Bohaty, S.M., Hodell, D.A., Laskar, J. and Zeebe, R.E. (2018a) Late lutetian thermal maximum—crossing a thermal threshold in earth's climate system? *Geochem. Geophys. Geosyst.*, 19, 73–82.
- Westerhold, T., Röhl, U., Donner, B. and Zachos, J.C. (2018b) Global extent of early eocene hyperthermal events: a new pacific benthic foraminiferal isotope record from shatsky rise (ODP Site 1209). *Paleoceanogr. Paleoclimatol.*, 33, 626-642.
- Westerhold, T., Marwan, N., Drury, A.J., Liebrand, D., Agnini, C., Anagnostou, E., Barnet, J.S.K., Bohaty, S.M., De Vleeschouwer, D., Florindo, F., Frederichs, T., Hodell, D.A., Holbourn, A.E., Kroon, D., Lauretano, V., Littler, K., Lourens, L.J., Lyle, M., Pälike, H., Röhl, U., Tian, J., Wilkens, R.H., Wilson, P.A. and Zachos, J.C. (2020) An astronomically dated record of Earth's climate and its predictability over the last 66 million years. *Science*, **369**, 1383–1387.
- Widdel, F. (1988) Microbiology and ecology of sulfate-and sulfur-reducing bacteria. In: Biology of Anaerobic Microorganisms (Ed. Zehnder, A.), pp. 469–585. Wiley, New York, NY.

- Xie, Q., Chen, T., Zhou, H., Xu, X., Xu, H., Ji, J., Lu, H. and Balsam, W. (2013) Mechanism of palygorskite formation in the Red Clay Formation on the Chinese Loess Plateau, northwest China. *Geoderma*, 192, 39–49.
- Yao, T., Zhu, H., Fu, B., Du, X., Wang, Q., Li, S., Yang, X. and Sánchez-Román, M. (2024) Origin of Eocene lacustrine dolomite and evolution of multiple diagenetic fluids in the Huanghekou sag, Bohai Bay Basin, China. *AAPG Bull.*, **108**, 1957–1984.
- Zaaboub, N., Abdeljaouad, S. and López-Galindo, A. (2005)
 Origin of fibrous clays in Tunisian Paleogene continental deposits. J. African Earth Sci., 43, 491–504.
- Zecchin, M. and Catuneanu, O. (2013) High-resolution sequence stratigraphy of clastic shelves I: Units and bounding surfaces. *Mar. Petrol. Geol.*, **39**, 1–25.
- Zentmyer, R.A., Pufahl, P.K., James, N.P. and Hiatt, E.E. (2011) Dolomitization on an evaporitic Paleoproterozoic ramp: Widespread synsedimentary dolomite in the Denault Formation, Labrador Trough, Canada. Sed. Geol., 238, 116–131.
- Zhang, F., Xu, H., Konishi, H., Kemp, J.M., Roden, E.E. and Shen, Z. (2012a) Dissolved sulfide-catalyzed precipitation

- of disordered dolomite: Implications for the formation mechanism of sedimentary dolomite. *Geochim. Cosmochim. Acta*, **97**, 148–165.
- Zhang, F., Xu, H., Konishi, H., Shelobolina, E.S. and Roden, E.E. (2012b) Polysaccharide-catalyzed nucleation and growth of disordered dolomite: A potential precursor of sedimentary dolomite. Am. Mineral., 97, 556–567.

Manuscript received 16 March 2025; revision accepted 10 May 2025

Supporting Information

Additional information may be found in the online version of this article:

Table S1. X-Ray Diffraction data.

Table S2. Carbon isotope data.